

STUDENTSKÁ PŘEHLÍDKA

Z HISTORIE

DISERTAČNÍ PRÁCE NA ČESKÉ UNIVERSITĚ V OBDOBÍ 1910 - 1950 ZAMĚŘENÉ NA ZKOUMÁNÍ PAPRSKŮ (A PAPRSKY) X

Ludmila Dobiášová

X-ray thesis presented in Czech University from 1910 to 1950. The first lecture „On X-rays“ was given in Czech University in 1914 by Prof. Závíška. In 1916, J. Novák presented his thesis „X-rays“. The problems of X-ray investigations were very broad because many devices were „home made“. The outstanding merit for development of X-ray research in the Czechoslovakia was brought Prof. J. Dolejšek and his school.

Disertační práce předkládaná na konci studií prokazuje způsobilost absolventa university, nejen, že získal odborné znalosti, ale že je schopen vědecky pracovat a dosažené výsledky zpracovat do přesně formulovaného odborného textu. Při volbě námětu disertační práce vychází uchazeč zpravidla z problematiky, která je v daném oboru středem pozornosti jeho školitelů. Soubor disertací v určitém období tak umožňuje poznat směr vědeckého bádání na universitě.

Pojďme se podívat, jaká byla témata prvních disertačních prací, které se nějakým způsobem dotýkaly paprsků X.

Na filosofické fakultě české university byly v letech 1882 - 1920 podávány disertace jak z humanitních, tak z přírodních věd, kde většinu tvořily práce z popisné geologie a geografie. Na filosofické fakultě platil v té době rigorosní řád z roku 1872. Státní zkoušky dávaly plnou aprobaci absolventům fakulty, kteří v převážné většině odcházeli učit na střední školy. Doktorát měl cenu hlavně pro ty absolventy, kteří předpokládali, že se uplatní za hranicemi. K dosažení doktorského titulu musela být předložena disertace a teprve její přijetí otevíralo kandidátům přístup ke složení dvou rigorosních zkoušek. Psaná nebo tištěná rozprava měla obsahovat pojednání z oboru přednášeného na fakultě a kandidát v ní měl - v přiměřené stylistické úpravě - projevit dokonalou znalost předmětu a samostatnost úsudku. Dvouhodinová zkouška z odborné specialisace vycházela z problematiky disertační práce, jednohodinová zkouška byla z filosofie. Za posouzení práce zaplatil kandidát dvěma referentům po 20ti zlatých, za rigorosa platil 40 a 20 zlatých.

V článku věnovaném počátkům rentgenové strukturní analýzy v českých zemích, uvádí autorka E. Těšínská [1], že první přednáška „O paprscích Röntgenových“ byla vypsána na české universitě prof. Závíškou v letním semestru roku 1914, tedy 9 let po jejich objevu. Ve školním roce 1916 podal Josef Novák v té době 28letý, disertační práci nazvanou „Paprsky X“. Školiteli mu byli profesori Strouhal a Kučera. V následujícím školním roce 1917 před-

ložil Rudolf Šimůnek disertační práci nazvanou „Interference Roentgenových paprsků“. Tuto práci si můžeme, na rozdíl od předchozí, prohlédnout v Archivu UK. Obsahuje 62 stran ručně psaného textu a 1 stranu obrázků.

V úvodu se seznámíme s popisem „mřížky prostorové“, s definicí krystalického stavu: „*A tak můžeme jako Groth definovati stav krystalický takto: krystal je homogenní (t.j. ve velmi malých vzdálenostech) periodicky uspořádané těleso, skládající se z atomů, a to tak, že jejich těžiště tvoří několik mřížek prostorových vzájemně se pronikajících...*“ Je zde i vysvětlení, proč jsou paprsky Roentgenovy vhodné pro zkoumání krystalů i stručný popis experimentu. V dalších oddílech jsou popsány teorie Laue a Bragga a vysvětlena jejich souvislost. Autor se zabývá „*strukturou NaCl, ZnS z polohy bodů na fotogramu Laueově a vlivem pohybu tepelného na interferenční zjevy Roentgenových paprsků*“.

V roce 1920 byla založena na české universitě samostatná přírodovědecká fakulta. Požadavky na úroveň disertací byly převzaty z řádu pro filosofickou fakultu, v novém předpise se navíc zmiňovalo, že práce má být samostatně vypracována a „*pouhá kompilace nestačí*“. Mezi dvěma světovými válkami platil kandidát za posouzení disertace 200.- Kč a rigorosní taxa byla 280.- a 140.- Kč. Tento řád byl užíván až do roku 1953.

V zimním semestru v roce 1922/23 vypsál prof. B. Ježek přednášku „*Souměrnost a röntgenometrie krystalů*“ [1]. Od této doby se přednášky i „*cvičení röntgenografické a röntgenometrické*“ objevují každý rok. Zájem profesorů o paprsky X a o novou metodu zkoumání vnitřní stavby hmoty se projevil i ve vyšším počtu diplomových prací věnovaných tomuto oboru. Protože převážná většina disertačních prací není fyzicky dosažitelná, můžeme na obsah prací usuzovat jen z jejich názvu, které jsou uvedeny v publikaci [2]. Názvy prozrazují, že se kandidáti neomezovali jen na výpočty a teoretické studie, ale že si museli poradit i s konstrukcí přístrojů a vším, co s danou metodikou souviselo (např. i s přípravou mazu používaného k utěsnění komor).

V roce 1925 podal Josef Hrdlička disertační práci „*O poměrech citlivosti bromostříbrných desek pro různé gradací intervaly v X spektrech*“. V roce 1927 předkládá disertační práci „*Experimentální studium rezonanční absorpce mědi v oboru X spekter*“, 36-ti letý Petr Skulari, který se později stal uznávaným odborníkem v aplikaci rentgenové difrakce v metalurgii. Spolu s ním podává disertační práci „*O malých mřížkových konstantách*“ i Artur Pavelka. Jeho úkolem je „*vybrati z některých jiných krystalů, jichž mřížkové konstanty jsou přibližně známy z prací mineralogů takové, jichž bylo by lze též použiti jako mřížek v X spektroskopii...*“ Na 24 stranách textu a tabulek psaných na stroji se podrobně zabývá i popisem experimentu a uvádí, že „*Velkým počtem měření a uvedenou metodou výpočtu nahraňuje množství zpracovaného materiálu pracně sice, ale měrou dostatečnou precísní stroje jinde používané, kterých nemáme...Poznámka k počtu měření...Jest tedy materiál tabulky I výsledkem 8,36 t.j. více než 280 jednotlivých měření z 8 různých snímků...*“

Od roku 1928, kdy se na pracích jako školitel začal podílet prof. Václav Dolejšek, vzrostl počet disertací, zabývajících se studiem fyzikálních vlastností paprsků X.



V roce 1931 obhájí Adéla Němejcová (provdaná Kochanovská, jedna z vůdčích osobností československé krystalografie) disertaci „*Studium inverzních účinků některých záření na fotografickou desku*“. Ve stejném roce podala Běla Gautschová pod vedením školitelů Němce a Vilhelma práci nazvanou „*Vliv Roentgenova záření na vzrůst a dýchání rostlin*“.

„*Nová metoda pro přesné měření mřížkové konstanty krystalů*“ je název disertace z roku 1934 ve které Josef Köppel na 52 stranách strojem psaného textu popisuje odlišnost a výhody nově vyvinuté metody, oproti metodě Siegbahnově. ...“ *V této práci uvádíme novou metodu pro přesné měření mřížkových konstant. Zatím co většina metod měří přímo úhel φ pro Braggův vztah, užívá naše metoda veličiny K rovné číselně rozdílu odrazových úhlů $\varphi_n - \varphi_m$ pro dva různé řády m, n téže linie. Metoda tato vznikla kombinací principu metody Pavelkovy (A.Pavelka Bull.int.de l'Acad. Des Sciences de Boheme 1927) se způsobem odečítání úhlů u metody Siegbahnovy. Byly uváženy všechny podmínky přesného měření zvláště Braggova fokusační podmínka, a shledáno, že projevy nedokonalosti Braggovy podmínky jsou u metody nové daleko menší nežli u metod měřících přímo úhel φ . Byl nalezen aproximativní vztah mezi fiktivními hodnotami mřížkové konstanty metody nové a reálnou mřížkovou konstantou. Prostudován charakter těchto fiktivních mřížkových konstant a shledáno, že jsou v konečném počtu a že jsou závislé na vlnové délce. Pro experimentální verifikaci nové metody užit přesný spektrograf Siegbahnův pro střední délky vln. Jako zdroje použito lampy typu Dolejšek-Valouch napájené usměrněným proudem.*“.

V roce 1938 předložil Jaroslav Feifer práci „*Měření vad krystalů double-crystal spectrometrem s fotografickou registrací*“.

Za 2. světové války, kdy byly vysoké školy zavřené, se přenesl rentgenografický výzkum do laboratoří průmyslových podniků a zaměřil se na praktické potřeby výroby. Spojení s praxí pokračuje i po válce, což vyjadřuje i název práce „*Stanovení krystalografické orientace křemenných destiček k piezoelektrickým účelům metodou Seemanova spektrografu*“, podané v roce 1946 Josefem Benešem. Ve stejném roce podává práci „*O hranici citlivosti registrace spekter X metodou čítače*“ Alois Brandejský. Účinky paprsků X na organickou hmotu se zabývá práce M.Sosny „*Vliv paprsků X na plasty*“ (1949), a V.Čeledová zkoumá „*Vliv roentgenova záření na vitalitu prvoků*“ (1950).

Přestože z některých názvů prací nelze jednoznačně určit jejich zaměření, můžeme předpokládat, že se první disertace věnovaná studiu paprsků X se objevila v roce 1916 a až do roku 1928 se touto tematikou zabývala každoročně 1 práce. V letech 1928 až 1939 vzrostl počet prací věnovaných studiu paprsků X nebo problematice spojených s jejich využitím na 2–4 ročně. Měl na tom zásluhu prof. Václav Dolejšek (1895-1945), který byl nejen světově uznávaným odborníkem, ale i silnou osobností. Zaujetí a nadšení pro svůj obor dovedl přenášet na mladé spolupracovníky a vytvářel jim stimulující podmínky k vědecké práci. V období let 1945-1950 se projevuje praktické zaměření disertačních prací a také rozšíření výzkumu účinku paprsků X na biologický materiál.

Literatura:

1. E. Těšínská, Materials Structure, 6 (1999).
2. Disertace pražské university 1882 – 1953, 1, UK, Praha 1965.

Biology, macromolecular crystallography

CRYSTALLIZATION AND PRELIMINARY X-RAY ANALYSIS OF RIBONUCLEASE / INHIBITOR COMPLEXES

Vladena Hlinková, Ľubica Urbániková, Jozef Ševčík

Institute of Molecular Biology, Slovak Academy of Sciences, Dúbravská cesta 21, 84251 Bratislava, Slovak Republic

The formation of complexes between proteins plays a major role in many biological processes, as for example antibody-antigen recognition, enzyme inhibition, inter- and intra-cellular transport. Knowledge of three-dimensional structures of the complexes facilitates better understanding of protein-protein recognition and could help in constructing specific inhibitors and drugs. Ribonucleases and their inhibitors represent very good model objects for this study. We have studied complexes of extracellular RNases Sa, Sa2 and Sa3 [1, 2] with three inhibitors: SaI14 and SaI20 isolated from *Streptomyces aureofaciens* [3] and barstar, specific inhibitor of barnase, a ribonuclease from *Bacillus amyloliquefaciens* [4]. The inhibitors form 1:1 non-covalent complexes with ribonucleases [5, 6]. The structures of the barnase/barstar and Sa/barstar complexes have shown that barstar sterically blocks the active site of the enzymes and the complexes are stabilized mostly by hydrogen bonds, charge interactions, and van der Waals contacts [7, 8, 9].

The complexes of Sa2/barstar and Sa3/barstar were crystallized by vapour diffusion method. The purity of all proteins was proved by a single band on the SDS electrophoresis and spectrophotometrically by $A_{278/252}$ ratio 2.0 for barstar, and 3.0 for Sa2 and Sa3, respectively. Crystals of the Sa2/barstar complex were grown from 0.2 M phosphate buffer at pH 7.0. The concentration of each protein was 6.5 mg/ml. As a precipitant 12 % PEG 8000 with 0.1 M ammonium sulphate were used. Dimensions of the crystals were about 0.4 x 0.2 x 0.2 mm. Crystals of the Sa3/barstar complex were obtained in 0.05 M imidazol-HCl buffer at pH 6.2, the concentration of both proteins was 6.5 mg/ml. As a precipitant 0.1 M NH_4Cl with 6% PEG 8000 were used. They have dimensions about 0.4 x 0.2 x 0.05 mm. The presence of both proteins in the crystals was confirmed by native electrophoresis.

Inhibitors SaI14 and SaI20 were overproduced in *E. coli* with the yield of about 100 mg of purified proteins from one litre of culture media. Complex of Sa3/SaI14 was



crystallized in 0.1 M HEPES at pH 8.0 with 1.6 M Li_2SO_4 used as precipitant. In spite of optimal pH value for complex formation in the crystallization solution, surprisingly, only Sa3 crystals were obtained with dimensions about $0.15 \times 0.15 \times 0.6$ mm. The data were collected at 100 K to 2.0 Å resolution using EMBL - Hamburg X31 beamline. As a cryoprotectant 23 % of glucose in precipitant solution was used. The crystals of Sa3 belong to trigonal space group $P3_121$ with unit cell parameters $a = b = 64.7$, $c = 69.6$ Å; $\gamma = 120^\circ$. The structure refinement is under way.

The crystals of Sa/SaI20 complex were obtained from 0.08 M HEPES at pH 7.4 and 0.8 M ammonium sulphate as a precipitant. The concentration of each protein in the drop was 5 mg/ml. Native data were collected at 100 K to 1.3 Å and anomalous data with Br⁻ ions to 1.6 and 1.5 Å resolution. For native data crystallization solution enriched by glycerol in 22 % concentration was used as a cryoprotectant. For anomalous data the crystal was soaked in the above solution containing in addition 0.6 M NaBr [10]. Data were collected at EMBL -Hamburg X31 beamline. Crystals belong to P222 space group with unit cell parameters $a = 38.2$, $b = 64.2$, $c = 77.1$ Å. The structure determination using MAD techniques is under way.

References

1. Ševčík, J., Dauter, Z., Lamzin, V.S. & Wilson, K.S. *Acta Cryst.* **D52**, (1996) 327-344.
2. Hebert, E.J., Grimsley, G.R., Hartley, R.W., Horn, G., Schell, D., Garcia, S., Both, V., Ševčík, J. & Pace, C.N. *Prot. Expr. Purif.* **11**, (1997) 162-168.
3. Krajčiková, D., Hartley, R.W. & Ševčík, J. *J. Bacteriol.* **180**, (1998) 1582-1585.
4. Hartley, R.W. *Trends Biochem. Sci.* **14**, (1989) 450-454.
5. Hartley, R.W. *Biochemistry* **32**, (1993) 5 978-5 984.
6. Hartley, R.W., Both, V., Hebert, E. J., Homerova, D., Jucovic, M., Nazarov, V., Rybajlak, & Ševčík, J. *Prot. Pept. Lett.* **3**, (1996) 225-331.
7. Guillet, V., Laphorn, A., Hartley, R.W. Mauguen, Y. *Structure* **1** (1993) 165-177.
8. Buckle, A.M., Schreiber, G. Fersht, A.R. *Biochemistry* **33**, (1994) 8 878-8 889.
9. Ševčík, J., Urbanikova, L., Dauter, Z. & Wilson, K.S. *Acta Cryst.* **D 54**, (1998) 954-936.
10. Dauter, Z. & Dauter, M. *Structure* **9** (2001) 21-26.

CRYSTALLIZATION AND PRELIMINARY STRUCTURE ANALYSIS OF ALCALINE SERINE PROTEASE AL-20 FROM NESTERENCONIA SP

J. Vévodová¹, S. Bakhtiar², R. Hatti-Kaul² & X.-D. Su³

¹ National Centre for Biomolecular Research, Faculty of Science, Masaryk University, Kotlářská 2, CZ 611 37 Brno, Czech Republic

² Department of Biotechnology, Center for Chemistry and Chemical Engineering, Lund University, S-221 00 Lund, Sweden

³ Department of Molecular Biophysics, Center for Chemistry and Chemical Engineering, Lund University, S-221 00 Lund, Sweden

Microbial serine proteases are attracting widespread attention due to their catalytic mechanism and digestion of other proteins. These enzymes are found in bacteria, eukaryotes and viruses [1]. The bacterial alkalophilic proteases make up a subgroup of subtilisin produced by a wide variety of alkalophilic bacteria. These enzymes are characterised by their activity at alkaline pH and their broad substrate specificity. Due to these remarkable properties, alkaline proteases have been used in several application such as food processing, leather tanning, protein-degrading additive to detergent, silver recovery and also as components in biopharmaceutical products.

These enzymes have been the subject of many protein engineering studies aimed at the extensively use in industrial application. Many protein engineering experience have been performed to design proteins that are active in extreme condition [2].

The enzymatic properties and three-dimensional structure of several member of this family of enzyme have been widely studied and a large body information has been assembled on their crystal structure [3]. All these enzymes share a common reactive centre composed of an oxyanion hole, a catalytic triad and an identical fold consisting of two antiparallel β -barrels [1].

The pure alkaline serine protease from *Nesterenconia* sp. was used for crystallization experiment. The crystals were grown by the vapour diffusion technique using hanging drop method. The crystallization conditions were screened using Hampton research crystallization kits. The crystals of the Al20 with suitable dimensions were used for data collection. Preliminary data for the unit-cell parameters and space-group determination were collected by crystallographic beamline BL711 at the MAX-Lab synchrotron in Lund using a MAR 345 image-plate detector and oscillation method. The crystals belong to the space group R3, with the unit cell parameters $a = 93.972$ Å, $c = 138.823$ Å, $\gamma = 120^\circ$. There are 2 molecules per asymmetric unit as estimated by the calculated value V_M [4], $2.681 \text{ Å}^3 \cdot \text{Da}^{-1}$. The solvent content for such a crystal is then approximately 52.35 %.

The determination of the three-dimensional structure by either molecular replacement and/or by multiple/single isomorphous replacement method, using the heavy atom derivatives (EMTS, K_2PtCl_4) is currently in progress.

1. Kuhn, P., Knapp, M., Soltis, M. S., Ganshaw, G., Thoene, M. & Bott, R., *Biochem.* **37** (1998) 13446-13452.
2. Cunningham, B. C. & Wells, J. A., *Protein Eng.* **4** (1987), 319-325.
3. Shirai, T., Suzuki, A., Yamane, T., Ashida, T., Kobayashi, T., Hitomi, J. & Ito, S., *Protein Engng.* **10** (1997), 627-634.
4. Matthews, B. W. (1968). *J. Mol. Biol.* **33**, 491-497.



STRUCTURAL BASIS OF THE HIV-1 AND HIV-2 PROTEASE INHIBITION BY A MONOCLONAL ANTIBODY

P. Řezáčová¹, J. Lescar², J. Brynda¹,
M. Fábry¹, M. Hořejší¹, R. Štouračová¹,
G. Bentley³ and J. Sedláček¹

¹*Department of Gene Manipulation, Institute of Molecular Genetics, Academy of Sciences, 166 37 Prague, Czech Republic,*

²*ESRF, BP220, F-38043 Grenoble, France*

³*Unité d'Immunologie Structurale, Dept. d'Immunologie, Institut Pasteur, 75724 Paris, France*

The HIV protease (HIV PR) is a homodimeric enzyme belonging to the family of aspartyl proteases. This enzyme plays an essential role in the HIV life cycle, and is thus one of the most attractive targets for design of specific inhibitors.

The murine monoclonal antibody (mAb) 1696, produced by immunisation with the HIV-1 protease, inhibits the catalytic activity of the enzyme of both the HIV-1 and HIV-2 isolates, with inhibition constants in the low nanomolar range. This antibody cross-reacts with peptides that include the N-terminus of the enzyme (residues 1-7), a region which is highly conserved in sequence among different viral strains and which, furthermore, is crucial for homodimerization to the active enzymatic form.

We report here the crystal structure of a recombinant single-chain Fv fragment of mAb 1696, expressed in *E. coli*, as a complex with a cross-reactive peptide from the HIV-1 protease at 2.7 Å resolution.

The antibody-antigen interactions observed in this complex provide a structural basis for understanding the origin of the broad reactivity observed between mAb 1696 with the HIV-1 and HIV-2 proteases and their respective N-terminal peptides. In addition, a possible mechanism of HIV protease inhibition by mAb 1696 is proposed that could help the design of inhibitors aimed at binding inactive monomeric species.

STRUCTURE ANALYSIS OF THE MUTATED HIV-1 PROTEASE WITH PEPTIDOMIMETIC INHIBITOR

Petr Skokan

Dept. of Solid Phase Engineering, Faculty of Nuclear Sciences and Physical Engineering, Czech Technical University; Břehová 7, 110 00 Praha 1

HIV protease was intensively studied during last several years. Inhibition of the HIV protease is one of the possibilities in the treatment of AIDS disease. The basic idea is to block the function of this enzyme, which plays important role in the maturation of the virus. Some commercial drugs like Saquinavir, Ritonavir, Amprenavir, Lopinavir, Nelfinavir, Indinavir introduced in last few years are based

on that principle. However, the virus gradually develops mutated forms of the HIV protease and thus the treatment loose efficiency. That is why mutated forms of the HIV protease receive high attention in the design of the new inhibitors.

X-ray diffraction is basic technique used in structure determination. Inhibitors were prepared at the Institute of Organic Chemistry and Biochemistry AS CR and protease at the Institute of Macromolecular Genetics AS CR. Crystals were prepared at the Institute of Macromolecular Chemistry AS CR. Example of the prepared crystals are on Fig. 1.



Figure 1. Example of the measured crystal (needle inside the loop)

Because of the small volume of the crystal it was necessary to use synchrotron X-ray source. Data up to 2.3 Å were collected at the ESRF Grenoble. Parameters of the micro-focus beamline: $\lambda = 0.934$ Å, 50 μm beam diameter, sample cooled by liquid nitrogen down to 100 K. Detector was MAR CCD detector with 165 mm diameter. Detail of the diffractometer is in Fig 2.

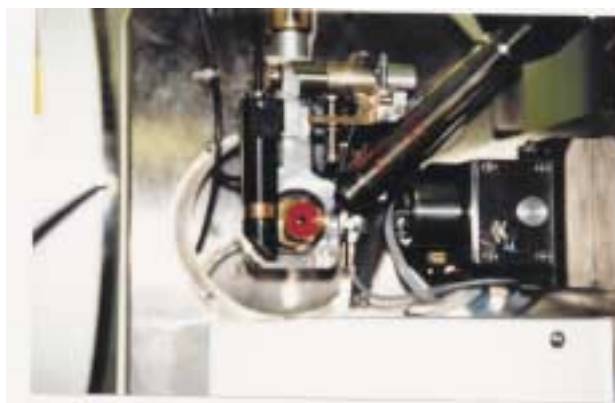


Figure 2. Detail of the diffractometer

HIV-1 protease forms active place in dimer (Fig 3.), each monomer contains 99 residues. In our case we have mutations in three places – A71V, I84V, V82I. Residues 84 and 82 are located in the active site of the protease and thus cause important steric change in the enzyme active site. Inhibitor is peptidomimetic Boc-Phe-ψ[(S)-CH(OH)CH₂-NH]-Phe-Gln-Phe (code-SQ, K_i = 33nM, Fig. 4).

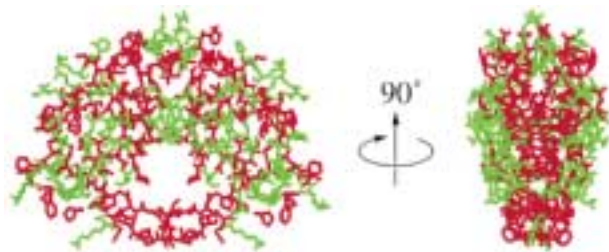


Figure 3. HIV-1 protease

Studied complex has crystallized in $P6_1$ space group, unit cell contains 6 dimers. Unit cell parameters are $a = b = 62.784 \text{ \AA}$, $c = 83.408 \text{ \AA}$; $\alpha = \beta = 90^\circ$, $\gamma = 120^\circ$. Starting model of the molecule was taken from previously determined structure of the similar complex in the same space group. Averaging gave 7976 symmetrically independent reflections with the data completeness 95 percent, $R_{\text{sym}} = 0.05$ (overall) and $R_{\text{sym}} = 0.26$ (shell 2.38-2.30 \AA). Starting R-factor of the model was 36 percent and it has dropped after few cycles of rigid body refinement to 29 percent. After restrained refinement and applying of the non-crystallographic symmetry, R-factor without inhibitor and water molecules dropped down to 25 percent. Refmac5 from CCP4 package is used for refinement and O program is used for visualisation. Refinement is still in progress.

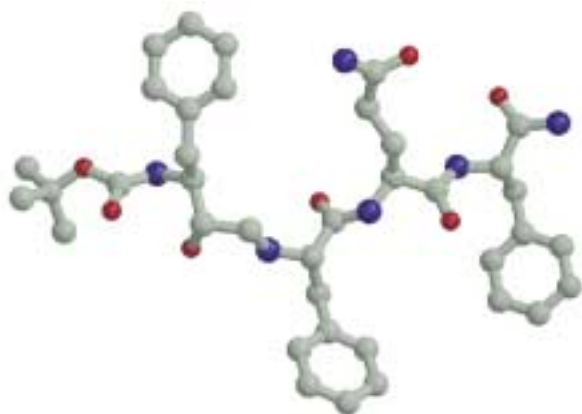


Figure 4. Inhibitor – SQ

The research is supported by the Grant Agency of the AS CR, project no. A4050811/1998 and Grant Agency of the Czech Rep., projects no. 203/98/K023; 203/00/D117; 204/00/P091

References:

1. Dohnálek, J., Hašek, J., Dušková, J., Petroková, H., Hradilek, M., Souček, M., Konvalinka, J., Brynda, J., Sedláček, J., Fábry, M. *A Distinct Binding Mode of a Hydroxyethylamine Isostere Inhibitor of HIV-1 Protease*. Acta Cryst. **D57**, 472-476.
2. J. Drenth *Principles of Protein X-ray Crystallography*, Springer-Verlag, New York 1994.
3. Software manuals: *HKL*, *Refmac5* and *O*.

AFFINITY OF HIV-1 PROTEASE TO TETRAPEPTIDE INHIBITORS

T. Skálová¹, J. Hašek¹, J. Dohnálek¹,
H. Petroková¹ and E. Buchtelová²

¹Institute of Macromolecular Chemistry AS CR,
Heyrovského nám. 2, 162 06 Praha 6, Czech Republic

²Faculty of Science, Charles University, Albertov 6,
128 43 Praha 2, Czech Republic

We study interaction between HIV-1 protease and a group of tetrapeptide inhibitors. Their symbols are explained in Fig.1. The experimental part of the project is aimed at X-ray structure determination of HIV-1 protease complexes with tetrapeptide inhibitors [1]. The theoretical part is a study of structure-activity relationship of these inhibitors using molecular modelling.

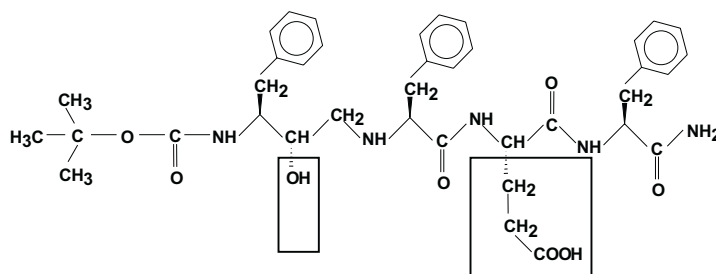


Figure 1. Scheme and symbols of studied inhibitors

OE = Boc-Phe- ψ [CH₂CH₂NH]-Phe-Glu-Phe-NH₂
 SE = Boc-Phe- ψ [S-CH(OH)CH₂NH]-Phe-Glu-Phe-NH₂
 SQ = Boc-Phe- ψ [S-CH(OH)CH₂NH]-Phe-Gln-Phe-NH₂
 SI = Boc-Phe- ψ [S-CH(OH)CH₂NH]-Phe-Ile-Phe-NH₂
 RE = Boc-Phe- ψ [R-CH(OH)CH₂NH]-Phe-Glu-Phe-NH₂
 RQ = Boc-Phe- ψ [R-CH(OH)CH₂NH]-Phe-Gln-Phe-NH₂
 RI = Boc-Phe- ψ [R-CH(OH)CH₂NH]-Phe-Ile-Phe-NH₂

HIV-1 protease

HIV-1 protease is composed of two chemically identical chains; each of them contains 99 residues. The active site is placed around Asp A25 and Asp B25, which play a crucial role in splitting of the substrate peptide bond. The active site is covered by flaps which form the binding tunnel with the active site in its center.

X-ray crystallography

Here we report the structure of mutant form of HIV-1 protease (A71V, V82T, I84V) in complex with the inhibitor OE. Diffraction data were measured at the synchrotron ESRF in Grenoble, beam line ID14-1, using wavelength $\lambda = 0.934 \text{ \AA}$. 73 images of 1° oscillations, 30 s exposition time and 150 mm crystal to detector distance have been processed. Data were processed using programs Denzo, Scalepack [2] and software package CCP4 [3]. Results are in Tab.1.

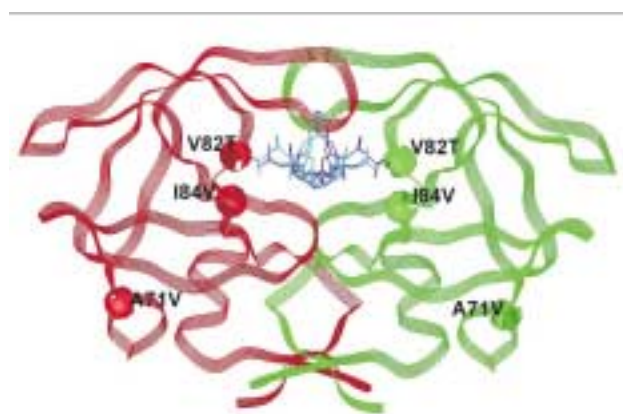


Figure 2. Mutated HIV-1 protease with OE inhibitor bound in two alternative positions

Table 1. Diffraction data parameters

Space group	P6 ₁
Unit cell: <i>a, b, c</i> [Å]	62.68 62.68 83.309
α, β, γ [°]	90 90 120
Resolution	33 - 2.2 Å
Number of measurements	61979
No. of unique reflections	9490
Completeness	99.9 %

The structure model is being refined using software package CNS [4]. The current R-factors before including solvent water molecules are $R = 24.7$, $R_{free} = 27.7$. The C_2 pseudo-symmetry of the protease is held by non-crystallographic symmetry restraints. The inhibitor is bound in two opposite orientations in the protease tunnel, which correspond with the C_2 pseudo-symmetry of the protease dimer.

Energetic considerations

The inhibition constant K_i defined as a ratio of concentrations of the protease, inhibitor and complex, $K_i = [PR][I]/[PR-I]$, is related to interaction energy E_{inter} between inhibitor and protease.

The experimental K_i was measured in vitro. Interaction energy is calculated as $E_{inter} = E(PR-I) - E(PR) - E(I)$. It is the energy of the complex (after minimization) minus the energy of the individual parts of the complex (without minimization). It means that the E_{inter} is equal to non-bonded energy between the protease and the inhibitor in the complex.

The minimized X-ray structures were taken as the input structure for the complexes of protease with the OE, RE, SQ inhibitors. The starting structures of complexes with inhibitors RQ, RI, SI, SE were modelled using X-ray structures of the complexes with RE and SQ.

In the search for economically acceptable procedure two different methods for calculation of interaction energy were tested:

Method 1 Software package: Discover in InsightII [6], force field: CFF91. The inhibitor was minimized in the protease fixed in the conformation found by X-ray diffraction.

Method 2 Software package: Discover in InsightII, force field: CFF91. The whole complex was minimized in three steps (hydrogen atoms minimized only, all atoms minimized except of backbone, all atoms of the complex minimized).

The third method using the software package Tinker [7] and force field MM3 has not shown good results and is not discussed in detail further here. The reasoning for better results obtained with CFF91 than with MM3 is that the force field CFF91 fully respects different types of amino acid residues (including N, C- terminus amino acids) and works well for the non-peptide inhibitors, too.

The results show that the procedure based on the inhibitor optimization only (with the protease geometry fixed in the position found from X-ray diffraction) gives comparable results with the procedure based on repeated minimization of the whole complex including the protease. The lower interaction energies between protease and inhibitors using the method 2 follow from better fit between flexible side chains of the protease and the conformationally restricted shape of the inhibitor.

The main advantage of the simplified method 1 is a large reduction of the computing time which falls for one calculation from days to hours giving thus the chance to test high number of drug candidates in reasonable time span.

In addition, the results show that the interaction energy does not play the decisive role in the fixation of inhibitor in the complex, at least for the peptidomimetic inhibitors that are the subject of our research. If the basic conditions for the realization of the most of the possible hydrogen bonds are fulfilled, the deformation energy necessary for fitting the inhibitor into the relatively well conserved shape of the protease active site and also the entropy connected with the residual conformational freedom of the inhibitor in the complex start to play the decisive role.

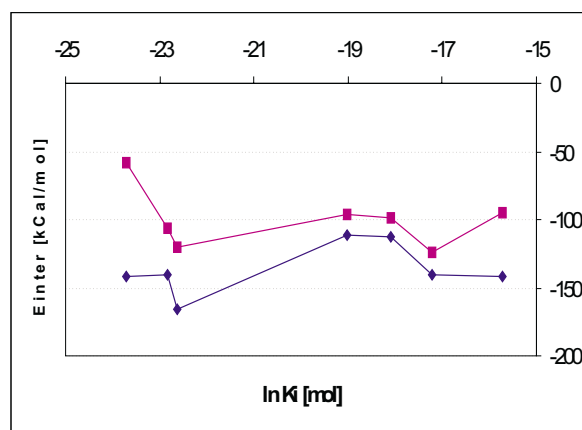


Figure 3. The dependence of the interaction energy on the logarithm of experimentally determined inhibition constants for inhibitors OE, RE, SE, RI, RQ, SQ, SI. ■... method 1, ◆... method 2

Acknowledgement: The research was supported by the project A4050811/1998 of the Grant Agency AS CR and projects of GA CR 203/98/K023, 203/00/D117 and 204/00/P091.

1. J. Dohnálek, J. Hašek, J. Dušková, H. Petroková, M. Hradílek, M. Souček, J. Konvalinka, J. Brynda, J. Sedláček & J. Fábry, *Acta Cryst.* **D57** (2001) 472-476.
2. Z. Otwinovski (1993), *Proceedings of the CCP4 Study Weekend: „Data Collection and Processing“*, 29-30 January 1993. Compiled by: L. Sawyer, N. Isaacs & S. Bailey, SERC Daresbury Laboratory, 56-62.
3. The CCP4 Suite: Programs for Protein Crystallography, *Acta Cryst.* **D50** 760-763.
4. A. T. Brunger, P. D. Adams, G. M. Clore, W. L. Delano, P. Gros, R. W. Grosse-Kunstleve, J. S. Jiang, J. Kuszewski, N. Nilges, N. S. Pannu, R. J. Read, L. M. Rice, T. Simonson & G. L. Warren, *Acta Cryst.* **D54** (1998), 905-921.
5. T. A. Jones, M. Kjeldgaard (1993). Manual for O version 5.9. Department of Molecular Biology, BMC, Uppsala University, Sweden; Department of Chemistry, Aarhus University, Denmark.
6. InsightII, Molecular Simulations Inc., 1995.
7. J. W. Ponder, TINKER – Software Tools for Molecular Design, version 3.6, Washington University School of Medicine, 1998.

PRODUCT OF AUTODIGESTION AT LEU63-ILE64 SITE BINDS TO HIV-1 PROTEASE INSTEAD OF INHIBITOR BOC-PHE-Ψ[(S)-CH(OH)CH₂NH]PHE-ILE-PHE-NH₂

E. Buchtelová¹, J. Hašek², J. Dohnálek², H. Petroková², J. Dušková², T. Skálová², J. Brynda³, J. Sedláček³, M. Hradílek⁴, J. Konvalinka⁴, E. Tykarska⁵, M. Jaskolski^{5,6} and L. Olivi⁷

¹Dept. of Biochemistry, Faculty of Science, Charles University, Prague, Czech Republic

²Inst. of Macromolecular Chemistry ASCR, Prague, Czech Republic

³Inst. of Molecular Genetics ASCR, Prague, Czech Rep.

⁴Inst. of Organic Chemistry and Biochemistry ASCR, Prague, Czech Republic

⁵A. Mickiewicz Univ., Poznan, Poland

⁶Center for Biocrystallographic Research, Inst. of Bioorganic Chemistry, PAS, Poznan, Poland

⁷Sincrotrone Trieste, Trieste, Italy

Human immunodeficiency virus 1 (HIV-1) protease enables the maturation of the HIV virus by processing of the viral polyprotein precursors with release of active enzymes

and structural proteins. A set of hydroxyethylamine inhibitors has been studied by our group in search for drugs active against resistant mutants of HIV-1 protease [1]. In course of crystallization trials with one of these, Boc-Phe-Ψ[(S)-CH(OH)CH₂NH]Phe-Ile-Phe-NH₂ [2], a crystal of HIV-1 protease complexed with an autoproteolysis product has been obtained. The HIV-1 protease undergoes autoproteolytic degradation at three major sites: Leu5-Trp6, Leu33-Glu34 and Leu63-Ile64 [3,4]. The structure we obtained contains a fragment of cleavage at the Leu63-Ile64 site.

Crystallization conditions: The inhibitor Boc-Phe-Ψ[(S)-CH(OH)CH₂NH]Phe-Ile-Phe-NH₂ was dissolved in DMSO and added to protease solution containing 6 mg/ml HIV-1 protease, 10 mM sodium acetate (pH 5.6), 1 mM EDTA and 0.5 mM DTT. The resulting concentration of inhibitor was 544 μM, twice the concentration of protease dimer. The resulting concentration of DMSO was 10%. The sample of protease was always kept below -45 °C before adding the inhibitor. The crystal on which data were collected grew at 4 °C one year after setting the crystallization experiment, in a hanging drop (1 μl protein sample + 1 μl reservoir solution) with reservoir solution of 0.88 M NaCl, 50 mM sodium citrate (pH 5.0) and 5% DMSO.

Diffraction data up to 1.8 Å were collected on a plate-shaped crystal of dimensions 0.1 x 0.1 x 0.01 mm at the beamline 5.2 of the ELETTRA synchrotron, Trieste, Italy, under cryo-cooling conditions (100K). The completeness of the data is 96.3%, which corresponds to 21072 independent reflections in the resolution range 20 Å – 1.8 Å; $R_{sym} = 4.9\%$. The crystals are orthorhombic, space group P2₁2₁2, with 4 molecules of the protease dimer per unit cell. The cell dimensions are $a = 57.8$ Å, $b = 86.3$ Å, $c = 45.8$ Å. The structure is being refined using the CNS package [5], the current values of R and R_{free} being 22.8% and 24.8%, respectively. About 70 water molecules have been included in the present model.

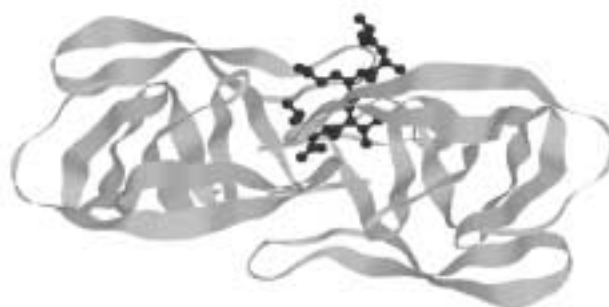


Figure 1. HIV-1 protease (gray) with the modeled product Ala-Asp-Gln-Ile-Leu-COOH (black) in the active site. The protease is viewed down the pseudosymmetry axis of the dimer. The product is covered by two β strands called flap (upper right part of the picture). The space below the pseudosymmetry-related flap (lower left part of the picture), belonging to the other monomer, is empty. If a substrate were bound to the protease instead of one of the products, its C-terminal part would lie here.

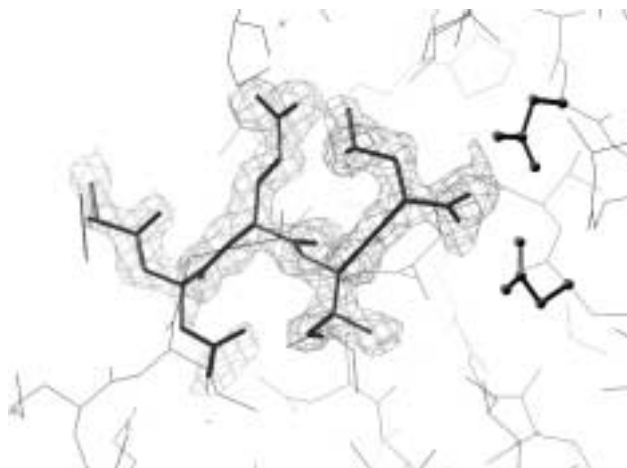


Figure 2. 2Fo-Fc omit map for the modeled product Ala-Asp-Gln-Ile-Leu-COOH. The map is drawn at 1.0 σ level. Part of the active site is shown (thin lines), with Asp25 and Asp25' (stick and ball model) in contact with the C-terminal carboxyl group of the product. All atoms of the product lie in the electron density except for C _{β} and C _{γ} of Asp60.

The fragment bound in the active site of the protease was identified from the electron density map as the N-terminal product of autoproteolytic cleavage of HIV-1 protease at the Leu63-Ile64 site. The inhibitor Boc-Phe- ψ [(S)-CH(OH)CH₂NH]Phe-Ile-Phe-NH₂ was not bound to the protease in the determined structure, even though the supposed concentration of the inhibitor (272 μ M in the hanging drop) exceeded about 1000 times its inhibition constant ($K_i = 0.150 \mu$ M at pH 4.7) [6], and was also higher than the concentration of protease (136 μ M in the hanging drop). The Michaelis constant of the peptide Arg-Glu-Tyr-Asp-Gln-Ile-Leu- \downarrow -Ile-Glu-Val-Ser, which has sequence identical to the Leu63-Ile64 autoproteolysis site of HIV-1 protease, is also higher (215 μ M at pH 5.5) [7]. We believe the most probable explanation is that the inhibitor concentration in the sample was decreased by precipitation which occurred after adding the inhibitor to the protease.

The cleavage product occupies one half of the active site, formed by one monomer of the protease homodimer (Fig. 1). In the other pseudosymmetrically related half of the active site, where the C-terminal product of cleavage could be bound, there is no continuous electron density into which the C-terminal product could be modelled. Some positive electron density comes up only in individual binding subsites (S1' and S2').

The N-terminal product makes contacts with the bottom of the active site as well as with one of the flexible flaps that cover the active site and form the protease tunnel. The product binds to the catalytic aspartates Asp25 and Asp25' in center of the active site via its C-terminal carboxyl. The electron density map for the three residues lying in the inner part of the active site, Gln61-Ile62-Leu63-COOH, is very clear (Fig.2). The preceding Asp60 is the last residue of the product that could be interpreted in the electron density map. Only an alanine residue has been modelled in the place of Tyr59. The rest of the product, lying outside of the active site of the protease dimer, is supposed to be disordered in the large cavity between neighboring protease dimers.

The research is supported by the Grant Agency AS CR project no. A4050811/1998 and GA CR projects no. 203/98-/K023, no. 203/00/D117 and no. 204/00/P091

1. J. Dohnálek, J. Hasek, J. Dušková, H. Petroková, M. Hradílek, M. Souček, J. Konvalinka, J. Brynda, J. Sedláček & J. Fábry, *Acta Cryst.*, **D57** (2001) 472-476.
2. E. Buchtelová, J. Hašek, J. Dohnálek, E. Tykarska, M. Jaskolski & L. Olivi, *Mater. Struct.*, **6** (1999) 6-7.
3. J.E. Strickler, J. Gorniak, B. Dayton, T. Meek, M. Moore, V. Maggaard, J. Malinowski & C. Debouck, *Proteins*, **6** (1989) 139-154.
4. J.R. Rose, S. Rafael & C.S. Craik, *J.Biol.Chem.*, **268** (1993) 11939-11945.
5. A.T. Brunger, P.D. Adams, G.M. Clore, W.L. DeLano, P. Gros, R.W. Grosse-Kunstleve, J.S. Jiang, J. Kuszewski, M. Nilges, N.S. Pannu, R.J. Read, L.M. Rice, T. Simonson & G.L. Warren, *Acta Cryst.*, **D54** (1998) 905-921.
6. J. Konvalinka, J. Litera, J. Weber, J. Vondrášek, M. Hradílek, M. Souček, I. Pichová, P. Majer, P. Štrop, J. Sedláček, A.M. Heuser, H. Kottler & H.G. Krausslich, *Eur. J. Biochem.*, **250** (1997) 559-566.
7. A.M. Mildner, D.J. Rothrock, J.W. Leone, C.A. Bannow, J.M. Lull, I.M. Reardon, J.L. Sarcich, W.J. Howe, C. S. Tomich, C. W. Smith, R. L. Heinrikson & A. G. Tomasselli, *Biochemistry*, **33** (1994) 9405-9413.

Abbreviations:

HIV-1, human immunodeficiency virus 1;

Boc, t-butoxycarbonyl;

DMSO, dimethyl sulfoxide;

EDTA, ethylenediaminetetraacetic acid;

DTT, dithiothreitol

Materials Science

KVANTITATÍVNA FÁZOVÁ ANALÝZA ŠTANDARDOV PORTLANDSKÉHO SLINKU

O. Pritula

Ústav anorganickej chémie Slovenskej akadémie vied, 842 36 Bratislava, Slovenská republika

Portlandský cement je zmesou veľkého počtu fáz. Najväčší vplyv na jeho konečné vlastnosti majú štyri fázy, ktoré sú v ňom aj najviac zastúpené. Týmito fázami sú Ca₃SiO₅ (C₃S), Ca₂SiO₄ (C₂S), Ca₂AlFeO₅(C₄AF) a Ca₉Al₆O₁₈ (C₃A). Doteraz nebola nájdená rýchla a presná metóda na stanovenie fázového zloženia cementu. Ako perspektívne sa javí vyhodnocovanie jeho rtg záznamu pomocou Rietveldovej metódy.

V našej práci sme sa snažili overiť vhodnosť použitia Rietveldovej metódy na rtg kvantitatívnu analýzu štandardných slinkov 8486, 8487 a 8488, ktorých zloženie je certifikované National Institute for Standards and Technology (NIST), USA. Pre každý z týchto slinkov sme namerali

dva záznamy. Jeden na difraktometri s reflexnou geometriou a druhý na difraktometri s transmisnou geometriou. Získané záznamy sme potom vyhodnocovali Rietveldovou metódou s použitím programu FULLPROF [1]. Do vstupného súboru sme použili tieto modely cementových fáz: C_3S monoklinický [2], C_2S monoklinický [3], C_4AF romboický [4] a C_3A kubický [5].

Každý záznam sme vyhodnocovali dvakrát. Najprv sme spresňovali škálovacie faktory, nulový bod, polšírky (W z $FWHM$), všeobecné teplotné a mriežkové parametre, prednostnú orientáciu (len v prípade C_3S) a obsadzovacie faktory (len v prípade C_4AF). Správnosť stanovenia klesala so znižovaním očakávaného zastúpenia jednotlivých fáz. S najväčšou správnosťou boli stanovené zastúpenia C_3S , s najnižšou správnosťou sme stanovili zastúpenia C_4AF a C_3A . V druhom cykle sme k spresňovaným parametrom pridali aj štruktúrne parametre jednotlivých fáz. Hodnota R_{WP} faktora sice poklesla o 1-8 %, správnosť stanovovania hmotnostných zlomkov jednotlivých fáz sa však nezvýšila.

Pri porovnávaní výsledkov spresňovaní pomocou záznamov, ktoré sme namerali na difraktometroch s rôznym usporiadaním, sme nepozorovali žiadne významné rozdiely vo vypočítaných zloženiach jednotlivých slinkov.

References

- Rodriguez-Carvajal J.: FullProf98. LLB 1998 (osobná komunikácia).
- Mumme W. G.: Crystal structure of tricalcium silicate from a Portland cement clinker and its application to quantitative XRD analysis. *Neues Jahrbuch für Mineralogie Abhandlungen*, **4** (1995) 145-160.
- Mumme W. G.; Hill R. J.; Bushnell - Wye G.; Segnit E. R.: Rietveld crystal structure refinements, crystal chemistry and calculated powder diffraction data for the polymorphs of dicalcium silicate and related phases. *Neues Jahrbuch für Mineralogie Abhandlungen*, **169** (1995) 35-68.
- Colville A. A.; Geller S.: Crystal structures of $Ca_2Fe_{1.43}Al_{0.57}O_5$ and $Ca_2Fe_{1.28}Al_{0.72}O_5$. *Acta Crystallographica*, **B28** (1972) 3196-3200.
- Mondal P. Jeffery J. W.: The crystal structure of tricalcium aluminate, $Ca_3Al_2O_6$. *Acta Crystallographica* **B24** (1968) 689-697.

ROLE OF TEXTURES IN TRANSFORMATION PROCESS IN CuAlMnZn SHAPE MEMORY ALLOY

D. Neov¹, P. Šittner² and P. Lukáš¹

¹Nuclear Physics Institute, ASCR, 250 68 Řež, Czech Republic

²Institute of Physics, ASCR, Na Slovance 2, Prague 8, 182 21, Czech Republic

The Shape memory alloys (SMA) are subject of continuous interest in material research because of their unique thermomechanical properties, [1], reversible inelastic strains up to several percents (Fig. 1) at which considerable

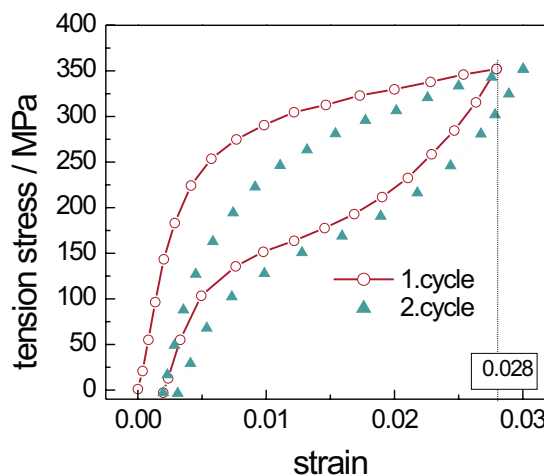


Figure 1. Typical reversible strain of CuAlMnZn observed in two mechanical cycles at constant temperature

amount of mechanical energy is released under temperature change. In addition, SMA generate high recovery forces upon heating and possess excellent dumping of mechanical vibrations or reversible shape change upon thermal loads. Commonly known as shape memory effects /SME/, all these phenomena derive from the thermoelastic martensitic transformation /MT/ induced by external mechanical or thermal loading. Among many of the currently investigated SMA, only NiTi-based, Cu-based and Fe-based alloys have commercial importance. The Cu-based shape-memory alloys have not so wide spread application as Ni-Ti based, but they exhibit strong transformation anisotropy, which manifests itself also in preferred formation of martensite phase. We have applied a new experimental technique for investigation of MT in SMA – in situ neutron diffraction stress/strain analysis of thermomechanically loaded SMA specimens [1]. The evolution of MT in deformation process can be significantly influenced by the effects of elastic and transformation anisotropy and textures, as well. However, *in situ* texture measurements are needed to obtain corresponding experimental data. In present work texture changes of Cu-10Al-5Mn-5Zn(wt.%) alloy are investigated by means of middle resolution neutron diffraction. Measurements of specimens under normal conditions, as well as under applied tensile stress were realized at LVR-15 research reactor in NPI Řež near Prague, Czech Republic. The bar specimen was step-wise loaded upon tensile stress. Diffraction spectrum was measured at each loading point. The results are compared with two-directional (axial and radial orientation with respect to the load axis) conventional TOF data collected by in-situ measurements of the same material performed on ENGIN instrument ISIS, Didcott, UK. Previous structural investigations report the presence of $L1_2$ ordered austenite in Cu-Al-Zn. In Cu-Al-Mn-Zn the structure evaluation can not produce exact information about the substitution of Cu atoms by the set of Al, Mn and Zn atoms sharing the same crystallographic positions. Fitting was done mainly by GSAS refinement packages as better suited for incorporation of texture information. Some calculations were done

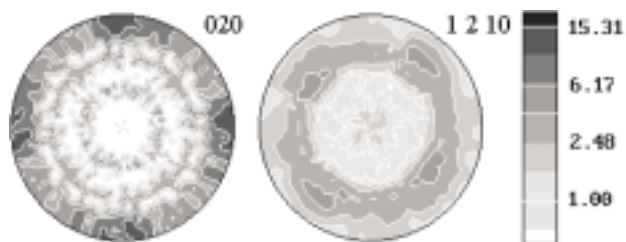


Figure 2. Pole figures of β_1' martensite (020) and (1210) reflections measured at the strain of 3%

by Fullprof program, as well. To refine the structure different diffraction probes like neutrons, X-ray and electrons are needed. The position ordering therefore smears and can not be observed. The structure of the parent austenite phase was fitted in $Im3m$ space group.

Because of certain technology steps during the sample preparation, initial strong axial texture is present in the samples. The commercially available SMA products as wires are typically fiber textured. The martensite phase exhibits also strong texture (Fig.2). Martensitic transformation processes in shape memory alloys are characterized by reversible texture transformations. Due to the lattice correspondence between austenite and martensite phases, this drawing texture is partially inherited upon transformation and possibly modified by preferential formation of martensite variants. However, the experiments and the computational simulations show the unique mutual relationship between the elastic anisotropy of the cubic austenite and transformation anisotropy of the stress induced $\beta_1 \rightarrow \beta_1'$ martensitic transformation which leads to redistribution of stresses in component grains preceding the onset of the large scale transformation flow in the polycrystal. As a result, most of the grains transform as the [110] and [100] except of the hardest grains with orientations close to the [111] (largest Young modulus E_{hkl} and transformation stress σ_{hkl}^{tr}) which transform only in the later stages of the tensile test.

References

1. D. Neov, P. Šittner, P. Lukáš, V. Novák, M. Vrána and P. Míkula, In-situ high resolution neutron diffraction study of stress induced martensitic transformations in CuAlZnMn shape memory alloy, The Fifth European Conference on Residual Stresses, 28-30 September 1999, Noordwijkerhout, The Netherlands, *Material Science Forum*, Vols. **347-349** (2000) p.334-339.

IN-SITU NEUTRON DIFFRACTION STUDIES OF MARTENSITIC TRANSFORMATIONS IN NiTi POLYCRYSTALS UPON THERMOMECHANICAL LOADING

D. Lugovoy¹, D. Neov¹, P. Lukáš¹ and P. Šittner²

¹Nuclear Physics Institute, 250 68 Řež, Czech Republic

²Institute of Physics, Na Slovance 2, Prague 8, 182 21, Czech Republic

Functional thermomechanical behaviors of martensitically transforming shape memory alloys are exploited for sensing, actuating or vibration control purposes in engineering applications. We have performed in-situ neutron diffraction experiments on NiTi polycrystalline alloy at dedicated stress/strain diffractometers equipped with thermomechanical testing device. The macroscopic data (stress, strain, temperatures) together with the diffraction data (lattice strains, phase compositions) collected during thermal, mechanical and thermomechanical recovery stress cycles characterize progress of the phase transformations processes between cubic B2 ordered austenite phase, rhomboedral R-phase and monoclinic B19' martensite phase in NiTi.

RTG DIFRAKČNÍ ANALÝZA DEFORMAČNÍCH STAVŮ

P. Neuman

Katedra materiálového inženýrství, fakulta metalurgie a materiálového inženýrství, Vysoká škola báňská – Technická univerzita Ostrava, 708 33 Ostrava-Poruba, Česká republika

Konvenční techniky nedestruktivního testování (NDT) – radiální, akustické, elektromagnetické, ... - jsou sice dobře zvládnuté, spolehlivě však fungují pouze jako nástroj zjišťování necelestvosti výrobků. Jestliže se zhoršení užitečných vlastností výrobku v průběhu jeho exploatace neprojevilo porušením jeho celistvosti, není prakticky metodami NDT zjistitelné a mnohé pokusy o aplikaci konvenčních metod nedestruktivního zkoušení v těchto případech nepřinesly uspokojivé výsledky. Optické (metalografické) metody jsou v tomto ohledu účinnější, ale jsou poměrně málo citlivé a indukují teprve změny, jež se projevují až v pokročilých stádiích degradace. Latentní degradace, která nepokročila natolik, aby už vznikly necelestvosti respektive rozsáhlé strukturální změny, patrné v mikroskopu, může být však velmi závažná neboť často vyústí v náhlé rozlomení a katastrofickou destrukci výrobku respektive celé konstrukce. Nebezpečí latentní degradace spočívá právě v tom, že je skrytá, tj. nezjistitelná konvenčními technikami NDT. Jindy bývá latentní degradace předstupněm degradace, která se manifestuje porušením celistvosti respektive rozsáhlými strukturálními změnami dřívě, než dojde ke katastrofické destrukci. V tom případě není sice

latentní degradace tak nebezpečná, ale její zjištění je přesto velmi užitečné, neboť umožňuje realizovat opravná opatření ještě dříve, než degradace pokročí natolik, že se stanou velmi nákladná.

Nejúčinnější technikou rozpoznávání a kvantifikace latentní degradace struktury materiálu je difrakce úzkého, co možná rovnoběžného svazku rtg záření, jež se „odráží“ (difraktuje) od jednotlivých krystalků. Na filmu pak dostaneme „reflexe“ (difrakční stopy), ze kterých vyčteme, jak je ten který krystalek velký, jaký má tvar, orientaci a strukturní defekty. Jedná se také o metodu nedestruktivní, která však na rozdíl od konvenčních způsobů NDT přináší informace o subtilních změnách struktury v měřítku (10 nm – 100 m), ke kterým při degradaci dochází mnohem dříve, než se objeví trhliny, zvětšení průřezu respektive masivní změny, jako tvorba precipitátů po hranicích zrn, jež lze zjistit světelnou mikroskopií in situ. Změny, které jsou na difrakčním obrazu struktury pozorovatelné v latentním stádiu degradace materiálu, výrazně ovlivňují tvárnost (křehkost) materiálu a svědčí o nestabilitě a procesech, jež se ve struktuře materiálu v průběhu jeho exploatace rozběhly.

Předmětem diplomové práce, o jejíchž výsledcích na kolokviu Struktura 2001 referujeme, bylo hledání korelací mezi plastickou deformací, mechanickými vlastnostmi, vzhledem mikrostruktury tak jak se jeví ve světelném mikroskopu a jejím difrakčním obrazem. Tato měření byla doplněna o stanovení tvrdosti. Ve své práci dokumentujeme, že v řadě případů taková korelace existuje a je velmi zřetelná. Tak jsme například prokázali, že sledováním azimutálního (laterálního) profilu difrakcí od krystalů feritu v dynamopleších můžeme monitorovat změny ve struktuře dynamoplechů, ke kterým dochází v důsledku postupného opotřebení raznice, pomocí níž jsou tyto plechy stříhány. Tyto změny spočívají v drčení (fragmentaci) krystalků, jež narůstá s opotřebením raznice. Do 40 000 stříhů je fragmentace sice zřetelná, ale malá, po 40 000 stříhů začne rozsah fragmentace prudce růst. Do 80 000 stříhů jsou fragmenty vzniklé rozdrčením původního zrna feritu v polotovaru většinou stále ještě větší než 10 μm . Po 80 000 stříhů postoupí fragmentace do kvalitativně pokročilejšího stádia a většina vznikajících fragmentů je už menší než 10 μm . Rtg difrakce tedy může být popsán způsobem využita pro optimalizaci rozhodování o tom, kdy by se měla nechat raznice znovu nabrousit.

X-RAY STUDY ON PLASMA-SPRAYED COATINGS Al_2O_3

Marek Liška

Department of Solid State Engineering, Faculty of Nuclear Sciences and Physical Engineering, Břehová 7, 115 19 Praha 1, Czech Republik

Atmospheric plasma-sprayed (APS) Al_2O_3 coatings are often used materials for their excellent chemical and thermal resistance. The nondestructive X-ray stress measurement requires X-ray elastic constants. The mechanical constants determined on compact ceramic are not applicable. To de-

termine the effective value of this elastic constants the applied strain by samples with various thickness of ceramic layer was measured. As a result, a strong strain-thickness relationship was obtained. Globally, the value of X-ray elastic constant of APS layer are higher than the one of compact ceramic. Qualitative phase analysis and a measurement of penetration depth were made.

1. Introduction

Protective Al_2O_3 scales are the basis for the high temperature oxidation resistance of many superalloys, metallic overlay coatings and thermal barrier coating (TBC) systems. Excellent thermal barrier coatings are required to increase an operating temperature in gas turbines. Coatings of alumina are applied for abrasion prevention because of their high hardness and strength and high thermal and corrosion resistance. This material is used for a large number of various engineering applications.

Mechanical stress in ceramic coatings on ductile substrates results as an interplay of series of stress generation and relief mechanisms during fabrication on the coating and under service conditions. Residual stresses in coatings are mainly caused by the thermal expansion mismatch strain between the coating and the substrate. Additional stresses arise due to substrate deformation, which are transferred to the coating. Large deformations of the ductile substrate can cause cracking and spalling of the brittle coating.

Since the residual stress in TBC films has a great influence on the interfacial debonding strength, X-ray method has been used to measure the residual stress. In most of previous works the mechanical elastic constants were used for calculating the stress from the measured lattice strain. Investigation on porous materials clearly show that X-ray elastic constant is much larger than the mechanical value. Therefore is necessary to measure experimentally the X-ray elastic constant in order to get an accurate stress value in TBC films. Knowledge of elastic constant in materials is an important step in the study of mechanical properties.

2. Experimental

2.1 Specimen and coating

The steel substrates of dimensions $80 \times 10 \times 2$ mm were used in the present study. Before spraying the surface of steel was pretreated by blasting with corundum grains. The mechanical adhesion between the alumina layer and substrate was improved by a NiCrAl binding layer with a thickness of 50 μm .

Ceramic coating were prepared by atmospheric plasma spraying, the spraying distance was 120 mm and substrate temperature 150 °C. The thickness of the sprayed coatings varied by spraying the layer in steps. Samples with coating thickness of 30 μm , 60 μm , 120 μm , 240 μm , 480 μm and 900 μm were produced. Thickness of 30 μm corresponds to one pass of the plasma spray gun.

2.2 Alumina phase analysis

Atmospheric plasma sprayed Al_2O_3 can exist in many crystallographic phases. Their qualitative analysis was performed by X-ray diffraction using both $\text{CrK}\alpha$ radiation and a $2\theta/\theta$ goniometer. The alumina coatings can be assumed to include α - and γ - Al_2O_3 phases. The results of the phase identification of the $900\ \mu\text{m}$ thick layer is in Figure 1.

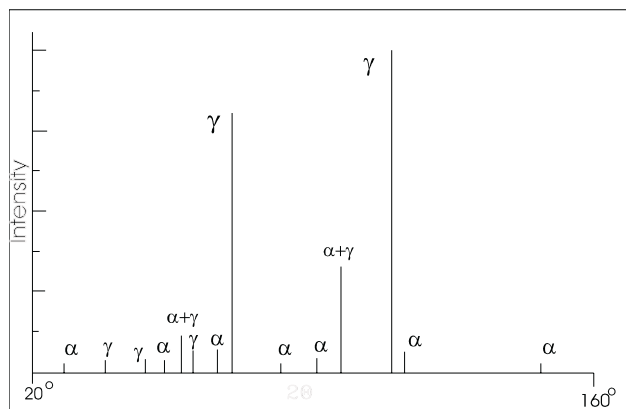


Figure 1. Phase diagram of Al_2O_3 atmospheric plasma sprayed layer

It is evident that the sprayed layer contains largely γ - Al_2O_3 with a remnant of α -phase.

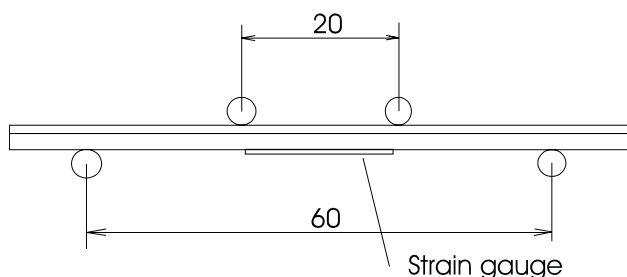


Figure 2. Schematic drawing of 4-point bending device

2.3 Penetration depth

The intensity of a peak from the binding NiCrAl layer was measured with varied thickness of the ceramic coating. The $2\theta_0$ angle of this diffraction line was 68° and the $\psi = 0^\circ$. The difference of intensity between a peak from free NiCrAl bending layer and bending layer with $30\ \mu\text{m}$ of alumina was 65%. The intensity of NiCrAl peak with $60\ \mu\text{m}$ alumina attained 5% of free sample intensity. This demonstrates that the observed penetration depth of CrK radiation is larger than the usually mentioned penetration depth in compact ceramic ($10\ \mu\text{m}$) [1]. It might be caused by porosity of the sprayed material (12%) and unevenness of the surface. In this penetration depth no stress gradient was observed. The relation between 2θ and $\sin^2\psi$ was linear.

2.4 Experimental techniques

The stress was measured by the X-ray „ $\sin^2\psi$ “ method. A diffractometer Siemens D5000 with a ψ -goniometer was used to measure the $\{440\}$ diffraction line centroid ($2\theta_0 =$

110°). Diffracted CrK radiation was detected by scintillation counter with a step scan of $0,1^\circ$ (2θ). The value of $\sin^2\psi$ was set from 0 to 0,8 with a step of 0,05.

The X-ray elastic constant $\frac{1}{2}s_2$ and s_1 are determined by:

$$\begin{aligned} \sigma_\varphi &= \frac{\theta - \theta_0}{\psi} \frac{\sigma_\varphi}{\theta} \\ &= \frac{\theta - \theta_0}{\sigma_\varphi} \frac{\theta}{\psi} \end{aligned}$$

where θ_0 is the diffraction angle of a stress-free specimen. The applied stress σ_φ must be uniaxial. Figure 2 illustrates the device used to apply an uniaxial stress to the specimen for X-ray measurement. The curvature of the bent plate is measured with the strain gauge on the reverse side. By using the above method the very small strain can be measured without contacting the film itself. The device can operate in both forward and reverse directions, so that the surface measured by X-rays can be both in tension and in compression, respectively.

3. Results and Discussion

3.1 Ceramic under tension

The sample in 4-point bending device was loaded up to 80% of value when the macroscopic cracks appeared. Within this range 15 values were obtained. The results of the measurement are in table 1.

In 900 and $480\ \mu\text{m}$ thick layer no increasing of stress was measured. The whole strain was concentrated in cracks and porosity. Only in the case of 60 and $120\ \mu\text{m}$ alumina layer stress increase was observed. An interesting development of deformation was measured. Crack propagation interrupted the deformation of the crystal lattice and stress relaxed to the value of residual stress. After the crack expansion the increase of stress started again. In the $30\ \mu\text{m}$ thick sample the error of $\sin^2\psi$ method was too vigorous to determine precisely a stress increase.

Table 1. Results of X-ray elastic constants of Al_2O_3 APS layer under tension

Thickness (μm)	$\frac{1}{2}s_2$ ($10^{-6}\ \text{MPa}^{-1}$)	s_1 ($10^{-6}\ \text{MPa}^{-1}$)
30	-	-
60	$19,3 \pm 0,9$	$-3,59 \pm 0,3$
120	$21,2 \pm 0,9$	$-3,94 \pm 0,3$
240	-	-
480	-	-
900	-	-

3.2 Ceramic under compression

The conditions of the measurement were identical to those of the tension experiment. The results are in Table 2. All samples were assumed to have the same elastic moduli 70

GPa, which was in agreement with mechanical and ultrasonic experiments. The decrease of stress was mainly evident in the case of small strain, by higher value of strain was no more fall of stress measured. The elastic constants

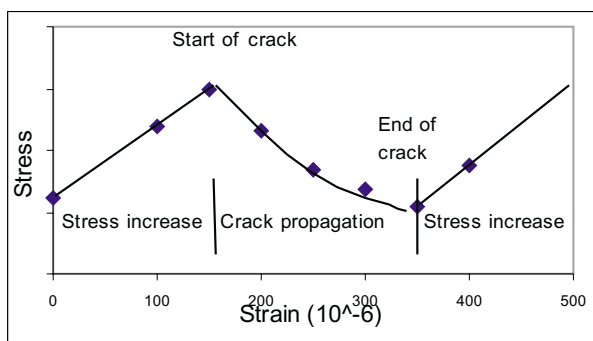


Figure 3. Stress measurement on 60 μm thick alumina layer under tension

by 60 μm thick layer differ from the development expected.

Table 2. Results of X-ray elastic constants of Al_2O_3 APS layer under compression

Thickness (μm)	$\frac{1}{2}s_2$ (10^{-6}MPa^{-1})	s_1 (10^{-6}MPa^{-1})
30	-	-
60	$16,3 \pm 0,9$	$-3,2 \pm 0,3$
120	$25,2 \pm 0,8$	$-4,7 \pm 0,3$
240	$18,2 \pm 0,4$	$-3,4 \pm 0,2$
480	$11,3 \pm 0,3$	$-2,1 \pm 0,1$
900	$7,9 \pm 0,3$	$-1,5 \pm 0,1$

3.3 Conclusions

The mechanically determined X-ray elastic constant for compact ceramic materials are $\frac{1}{2}s_2 = 3,01 \cdot 10^{-6} \text{MPa}^{-1}$ and $s_1 = -0,56 \cdot 10^{-6} \text{MPa}^{-1}$ [2]. The stress value calculated in APS layer by using this elastic constants can be much higher than the actual value.

The mechanical strain is the sum of strains of all phases constituting the ceramic layer, while the X-ray strain is the strain of the analysed crystalline phase. A small X-ray elastic constant means that the stress in the crystalline phase is smaller than the applied stress. Softer phases such as pores and micro-cracks existing in ceramic coating contribute to this difference. The surface roughness also contributes to this difference - this fact explains the unexpected small value of elastic constant (both tension and compression) by 60 μm thick layer. The decrease of elastic constant by the increase of the sample thickness is explained by the concentration of strain in noncrystalline phase of ceramic coating. The extreme case is thick samples tension experiment, where the whole strain is concentrated in porosity and cracks. Globally the value of X-ray elastic constants of APS Al_2O_3 layer is higher than the one of compact ceramic.

Acknowledgements

The author would like to thank H.-D. Tietz, L. Pfeiffer and U. Gieland of the Westsächsische Hochschule Zwickau for assistance with some of the experimental work and for various helpful discussions.

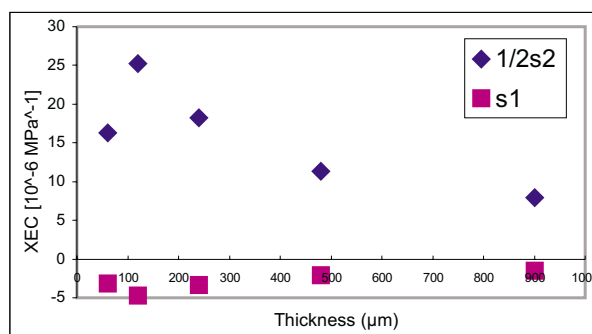


Figure 4. XEC-thickness relationship of Al_2O_3 APS layer under compression

References

1. Kraus I. Ganev N.: Difrakční analýza mechanických napětí, Vydavatelství ČVUT, Praha 1995
2. Hauk V.: Elastic Constants and Residual Stresses in Ceramic Coatings, ICRS – 2, Nancy 1988
3. Kraus I., Ganev N., Gosmanova G., Tietz H.-D., Pfeiffer L., Böhm S.: *Advanced Performance Materials* **4**, (1997) 63-69
4. Tietz H.-D.: Technische Keramik, VDI-Verlag GmbH, Düsseldorf 1994
5. Suzuki K., Machiya S., Tanaka K.: Proc. 5th ICRS, 2000
6. Eigenmann B., Scholtes B., Macherauch E.: *Mat.-wiss. und Werkstofftech.* **20**, (1989) 314-325

X-RAY STRUCTURE STUDY OF QUATERNARY COMPOSITES TiWCN

M. Dopita¹ and C. Kral²

¹Department of Electronic Structures, Faculty of Mathematics and Physics, Charles University, Ke Karlovu 5, CZ-121 16 Prague, E-mail: dopita@apollo.karlov.mff.cuni.cz

²Institute for Chemical Technology of Inorganic Materials, Vienna University of Technology, Getreidemarkt 9/161, A-1060 Vienna Austria.

The most general effort in production of cemented carbides and carbonitrides is devoted to the increase of their service time. One of the most successful achievements in this task was the deposition of thin films by CVD or PVD techniques. The first generation of such layers were single-phase layers such as TiN and TiC, followed by the second generation multiphase layers where a variety of compounds such as TiN, TiC, Ti(C,N), (Ti,Al)N and Al_2O_3 was combined. The third generation of materials consists of functional-gradient cemented carbonitrides. Such mate-

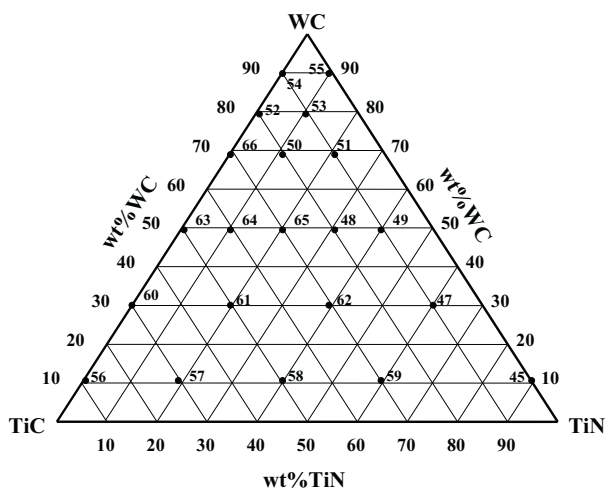


Figure 1. For investigation of the interaction of the Ti-W-C-N system with N_2 at 1773 K two different nitrogen pressures were applied. A first set of samples was annealed at 10 bar of nitrogen for 96 hours and a second set of samples was annealed at 30 bar for 66 hours.

rials have the benefit of thermal and mechanical load dissipation (because of a smooth variation of constituents in their microstructure) avoiding piling up of stresses at distinct interfaces. The surface roughness is only slightly higher than for coated materials and the residual stresses in the surface layers are in general compressive or zero.

A set of samples with different composition was prepared for investigation of the hard phases in the Ti-W-C-N system. (see Fig.1). The samples were made from well-analyzed TiC, TiN and WC powders, ball-milled half an hour in cyclohexane, dried and cold-pressed. To obtain dense specimens, the hot pressing was performed at 2573 K in inert Argon atmosphere. To obtain a thermodynamic equilibrium at 1773 K, the samples were annealed in Argon atmosphere (1 bar) for 168 hours.

The samples were analyzed using the glancing angle X-ray diffraction performed alternatively with the Seemann-Bohlin diffractometer or with the parallel beam optics. In both cases, the angle of incidence of the primary beam (γ) was 10 degrees, which corresponds to the penetration depth up to 10 μm , depending of course on the real composition of the samples.

Qualitative phase analysis was performed to obtain information about phases present in the samples. Generally these phases have been found: hexagonal W_2C , hexagonal WC, bcc tungsten (W), and one or two fcc TiWCN phases. The principal difference between the samples A (annealed at 10 bar) and B (annealed at 30 bar) was observed in positions of boundaries showing their phase stability. Particularly in set A, the range of coexistence of two face centered cubic phases is restricted just to the samples containing small amount of WC before annealing. On the other hand, in the B samples the phase boundary for the coexistence of two fcc phases reaches nearly to one half of the phase diagram. Additional important difference between both sets of samples appears in the areas where body centered cubic tungsten forms. In the set B, the presence of tungsten is restricted to the part of the phase diagram rich in TiN,

whereas in the set A, tungsten is present nearly in whole diagram except areas rich in TiC and WC.

Residual stress and stress-free lattice parameter were calculated for cubic phases from the dependence of the lattice parameters on the function $\sin^2\psi$ ([1], [2], [3], [5]). In the most samples, the residual stress in face centered cubic and in body centered cubic phases is small and has a compressive character. In the samples A, residual stress varies from -4 GPa to 2 GPa, and in the set B from -6 GPa to 2 GPa. The stress-free lattice parameter in the TiWCN phases is strongly dependent on the amounts of nitrogen and tungsten. In the samples, which were rich in TiC and TiN before having been annealed, two fcc phases were observed: both featured different values the of stress-free lattice parameters. In the hexagonal phases (W_2C and WC), lattice deformations were obtained from the changes in interplanar spacing as related to the stress-free interplanar spacing. The values of the stress-free interplanar spacing were taken from the PDF-2 [5]. We can draw a particular conclusion that one of these two phases has higher amount of tungsten than the other one, which contains more nitrogen. This is a consequence of low affinity of tungsten to nitrogen). The stress-free lattice parameter of the body centered cubic tungsten was smaller than the tabulated one in all cases, what might have been caused by the presence of a small amount of titanium embedded in the pure tungsten phase.

Finally, crystallite size and the micro-deformation were calculated from the dependence of the corrected integral breadth on the function $\sin \Theta$.

References

1. I. C. Noyan, J. B. Cohen: *Residual Stress*, Springer Verlag, Berlin, 1987.
2. A.J. Perry, V. Valvoda, D. Rafaja: X-ray residual stress measurement in TiN, ZrN and HfN films using the Seemann-Bohlin method. *Thin Solid Films* Vol **214** (1992) 169.
3. D. Rafaja, V. Valvoda, R. Kuzel, A.J. Perry, J.R. Treglio: XRD characterization of ion-implanted TiN coatings. *Surf. Coat. Technol.*, **86-87** (1996) 302-308.
4. D. Rafaja, V. Valvoda, A.J. Perry and J.R. Treglio: Depth profile of residual stress in metal-ion implanted TiN coatings. *Surf. Coat. Technol.* **92** (1997) 135-141.
5. Powder Diffraction File PDF-2.02, International Centre for Diffraction Data, 1999.

X-RAY SCATTERING ON SELF-ASSEMBLED QUANTUM WIRES IN Si-Ge MULTILAYERS

M. Meduňa¹, V. Holý¹, T. Roch², G. Bauer²,
O. G. Schmidt³ and K. Eberl³

¹Institute of Condensed Matter Physics, Masaryk University, Brno, Czech Republic

²Institut für Semiconductor Physics, J.Kepler University, Linz, Austria

³Max-Planck Institut für Festkörperforschung, Heisenbergstrasse 1, Stuttgart, Germany

The structural quality of semiconductor heterodevices is very important for achievement of their high electronic and optical performance. One of the important structure parameters is the elastic strain limiting the thickness of the heteroepitaxial layers. Under suitable growth conditions, this strain is relieved elastically and usually give rise to a periodic surface pattern of small islands (Stranski-Krastanov growth [1] or one-dimensional mesoscopic ripples (step bunching mechanism [2] - on vicinal surfaces). This phenomenon can be used for an efficient technology of low dimensional quantum structures.

The growth of the one-dimensional terraces can be described by a strain-induced bunching of monolayer steps. The resulting patterns are always perpendicular to the azimuthal direction of the substrate miscut. In case of kinetic roughening, which is present in homoepitaxial growth without strain, the situation is much more complicated. The orientation of the monoatomic steps depends substantially on the surface reconstruction. On a (001) surface with the 2x1 reconstruction, the monoatomic steps are oriented in two possible $\langle 110 \rangle$ directions [3]. However, the mean orientation of the step bunches is not connected with $\langle 110 \rangle$, it depends mainly on the miscut azimuth. If the miscut azimuth is along $\langle 110 \rangle$, the bunches are parallel to the monoatomic steps and perpendicular to the miscut direction, in other cases a more complicated zig-zag pattern of the steps on the surface can be expected. This zig-zag pattern forms the periodic ripples parallel to the miscut see Fig. 1.

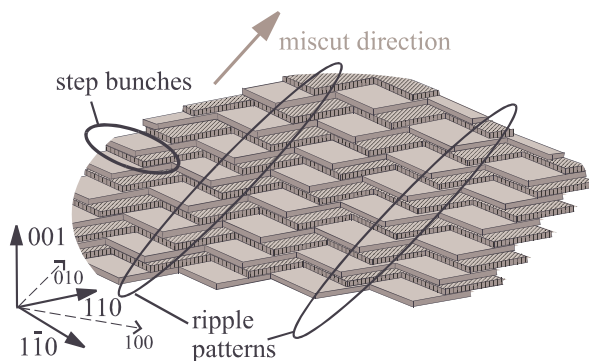


Figure 1. The zig-zag structure of the double steps forming periodic ripples along $\langle 100 \rangle$ direction

Previous results [4] show that the step bunches occur also on a surface of a homoepitaxial layer without internal stresses. In [5], a self-organized structure on the surface of a Si homoepitaxial buffer layer with the miscut oriented along $\langle 100 \rangle$ was investigated and a ripple-pattern has been found parallel to the miscut direction. This pattern was explained qualitatively by a combination of single monoatomic steps into so called double-steps creating a zig-zag structure, which consists of a sequence of mesoscopic ripples parallel to $\langle 100 \rangle$.

We have investigated the interface morphology of Ge/Si strained multilayers grown by molecular beam epitaxy (MBE) on Si(001) vicinal substrate. The azimuth of the miscut of Si substrate was intentionally declined from 100 direction by 15° . Series of five multilayers with different Si-spacer thicknesses were studied by means of x-ray specular and diffuse small angle reflection. The x-ray measurements have been carried out using a laboratory x-ray source equipped by a parabolic x-ray mirror and secondary monochromator. The surface structure has been observed by atomic force microscopy.

From the x-ray specular reflectivity data we determined the multilayer periods, from the non-specular reflectivity we have determined the morphology of the interfaces, giving us the information on shapes of the ripples and their in-plane arrangements. The diffuse scattering measurements were carried out in several azimuthal directions of the scattering plane, to prove the one-dimensionality of the ripples. Further details of the experiment and the sample preparation can be found in previously published papers [6] and [7].

The theoretical calculations of the diffuse scattering have been performed by means of the Distorted-wave Born Approximation (DWBA), assuming a self-affine sequence of hyperbolic ripples at the interface. The measurements and simulations indicate that the ripples are really oriented exactly parallel to the 100 direction; the dependence of the fitted parameters of the ripple structure on the growth time supports the kinetic roughening of the surface. These results and also atomic force microscopy studies indicate that the qualitative model of surface rippling developed for homoepitaxial Si growth may be valid for heteroepitaxy as well.

References

1. D. J. Eaglesham and M. Cerullo, *Phys. Rev. Lett.*, **64** (1990) 1943-1943.
2. F. Liu, J. Tersoff, and M., G. Lagally, *Phys. Rev. Lett.*, **80** (1998) 1268-1271.
3. E. Pehlke and J. Tersoff, *Phys. Rev. Lett.*, **67** (1991) 465-468.
4. N. E. Lee, D. G. Cahill, and J. E. Greene, *Phys. Rev. B*, **53** (1996) 7876-7879.
5. C. Schelling, G. Springholz, and F. Schäffler, *Phys. Rev. Lett.*, **83** (1999) 995-998.
6. M. Meduňa, V. Holý, T. Roch, G. Bauer, O. G. Schmidt, and K. Eberl, *J. Phys. D: Appl. Phys.*, **34** A193-A196.
7. O. G. Schmidt, O. Kienzle, Y. Hao, K. Eberl and F. Ernst, *Appl. Phys. Lett.*, **74** (1999) 1272-1274.



GRAZING INCIDENCE SMALL-ANGLE X-RAY SCATTERING FROM SELF-ORGANIZED ISLANDS AT SEMICONDUCTOR INTERFACES

O. Caha, M. Meduňa and V. Holý

Institute of Condensed Matter Physics, Faculty of Science, Masaryk University, 611 37 Brno, caha@physics.muni.cz

Quantum confinement of carriers in self-organized lateral structures at interfaces in semiconductor heteroepitaxial systems represents a very promising way for the fabrication of electronic and optoelectronic devices with unique properties. During the heteroepitaxial growth in so called Stranski-Krastanow growth mode [1], the growing surfaces becomes nearly periodically corrugated, which leads to a creation of small islands at the surface (self-assembled quantum dots).

The electronic and optical performance of these structures depends substantially on the homogeneity of their shapes and sizes. The only method suitable for *non-destructive* investigation of the shapes and sizes of *buried* dots below the surface is x-ray scattering. Small angle x-ray scattering is sensitive to local changes in electron density so that it can reveal the shape and size of the buried islands independently of their chemical composition. Wide-angle scattering (x-ray diffraction) is influenced mainly by the local elastic strain-fields around the islands and consequently, from the diffraction data the chemical composition of the islands can be deduced.

In the presented work, we have investigated buried and free-standing self-assembled quantum dots using grazing-incidence-small angle x-ray scattering method (GISAXS, Fig. 1). In this method, the primary monochromatic beam of synchrotron radiation (beamline ID01 at ESRF, wavelength 1.5 Å) irradiates the sample surface under a small angle of incidence α_i (comparable to the critical angle of total external reflection). A linear x-ray detector measures the distribution of the scattered intensity for various y -components of the scattering vector $\mathbf{Q} = \mathbf{K}_f - \mathbf{K}_i$. Changing the azimuthal direction of the plane of incidence (i.e. the direction of the x and y axes) and keeping constant the angles of incidence and exit $\alpha_{i,f}$ we obtain the distribution of the scattered intensity in the Q_x, Q_y plane in reciprocal space parallel to the sample surface.

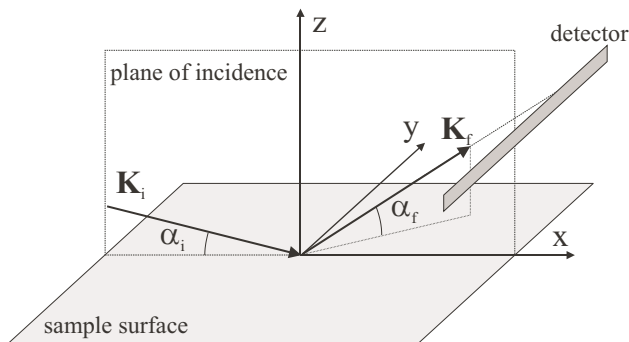


Figure 1. Sketch of the GISAXS method

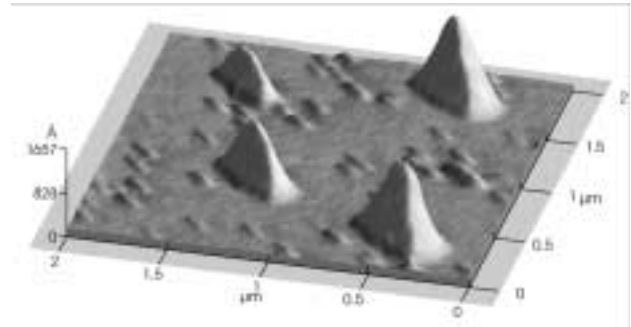


Figure 2. AFM of the the InAs/GaAs superlattice

Within the distorted-wave Born approximation (DWBA) [2] the distribution $I(\mathbf{Q})$ of the intensity diffusely scattered from buried islands is given by [3]

$$I(\mathbf{Q}) = \alpha_i \alpha_f \Omega(\mathbf{q}) |G(\mathbf{q})|^2 |T(\alpha_i, \alpha_f)|^2$$

where $G(\mathbf{q})$ is the Fourier transformation of the correlation function of the positions of the islands, $\Omega^{\text{FT}}(\mathbf{q})$ is the Fourier transform of the shape function $\Omega(\mathbf{r})$ of a single island (unity in the island and zero outside it), and $T(\alpha_i, \alpha_f)$ is transmission function of the sample surface. The vector \mathbf{q} is the scattering vector \mathbf{Q} corrected to the refraction at the sample surface. Similar formula is valid also for the free-standing islands.

We have investigated two types of samples:

1. Superlattice $7x[\text{InAs}(4.5 \text{ \AA})/\text{GaAs}(130 \text{ \AA})]$ grown on (001) GaAs by metallorganic chemical vapor deposition (kindly provided by dr. Hulicius, Inst. Of Physics CAS, Prague).
2. Superlattice $3x[\text{InP}(26 \text{ \AA})/\text{In}_{0.48}\text{Ga}_{0.52}\text{P}(150 \text{ \AA})]$ grown on a (001) GaAs substrate by liquid phase epitaxy (kindly provided by prof. R. Koehler, Humboldt University Berlin).

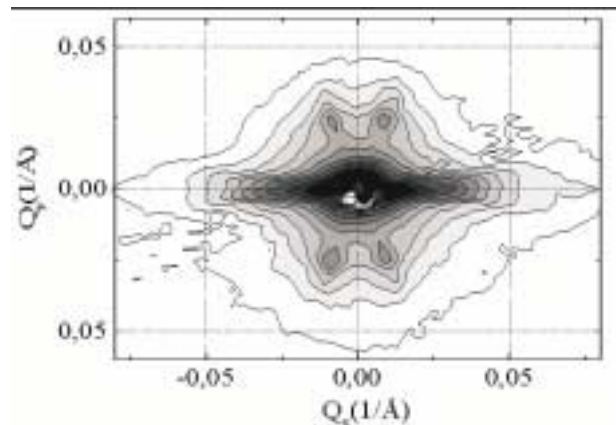


Figure 3. The measured GISAXS map of the InAs/GaAs superlattice

In the first case, the islands were laterally completely disordered so that the correlation function $G(\mathbf{Q}_{\parallel}, q_z = \text{const})$ exhibited no subsidiary intensity maxima. The AFM picture of the surface (see Fig. 2) revealed a bimodal distribution of the sizes of pyramidal islands at the surface. The GISAXS intensity map is shown in Fig. 3. The position of the four distinct subsidiary maxima in Fig. 3 scales linearly

with Q_z . Therefore, they are caused by the island shape and not by the correlation of island positions. In reciprocal space, these maxima lie along the normals to the sidewalls of the pyramids.

In order to compare the measured data with the simulations, we have extracted a line scan from the measured map crossing the subsidiary maxima. In Fig. 4., we compare the measured intensity scan with the simulation. From the comparison we have determined the size of the pyramid base to (400 ± 20) Å and the pyramid height to (170 ± 10) Å. These sizes refer rather to the buried pyramids, since their total number is much larger than that of the free standing ones.

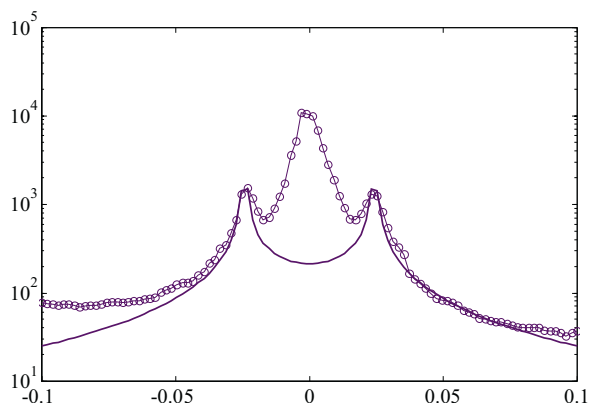


Figure 4. Line scan extracted from the experimental map in Fig. 3 (points) and its fit (full line)

The islands in the InP/GaInP superlattice are laterally correlated giving rise to subsidiary maxima, whose position is *independent* of Q_z . In order to extract the information on the island shape from the measured data, we performed a Fourier filtering method of the measured data. If we assume that the island size is much smaller than the mean distance of the islands, in the Fourier transformation of the measured map (i.e. in the intensity distribution in *real space*), the central peak is determined only by the shape of an individual island. In Fig. 5, the measured intensity map $I(Q_{||}, Q_z = \text{const})$ is plotted, Fig 6. shows the central peak of the two-dimensional Fourier transformation $I^{\text{FT}}(x, y, Q_z)$ along with its fit assuming an ellipsoidal island shape.

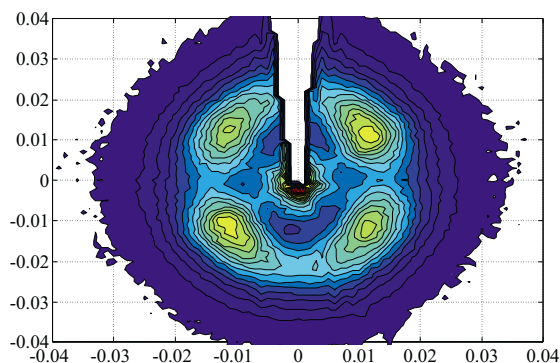


Figure 5. The GISAXS map of the InP/GaInP superlattice

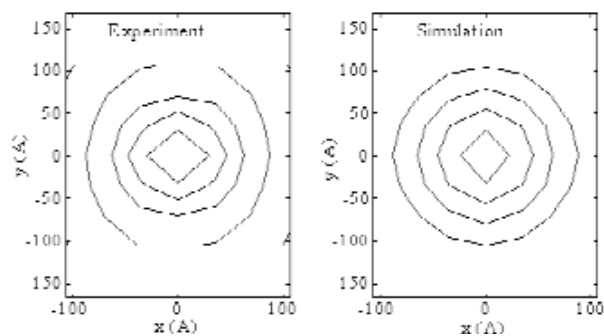


Figure 6. The central part of the Fourier transform of the map in Fig. 5 (left) and its simulation (right)

From the fit we determined the lengths of the horizontal half-axes of the ellipsoidal island to (84 ± 3) Å, (68 ± 3) Å, the island height is (10 ± 2) Å.

The work is still in progress. A series of maps measured at various Q_z makes it possible to detect the dependence of the island shape on the island depth below the sample surface and therefore, it might be possible to estimate the role of the interdiffusion on the shape of the buried islands.

1. see for instance A. P. Alivisatos, *Science* **271**, 933 (1996) and the references therein.
2. V. Holý., U. Pietsch and T. Baumbach, *High-Resolution X-Ray Scattering From Thin Films and Multilayers* (Springer-Verlag Berlin, Heidelberg, New York 1999).
3. J. Stangl, V. Holý, T. Roch, A. Daniel, G. Bauer, J. Zhu, K. Brunner, G. Abstreiter, *Phys. Rev. B* **62**, 7229-7236 (2000).

EVALUATION OF STRUCTURE PARAMETERS OF THIN LAYERS

Daniel Šimek^{1,2}, Jiří Kub², Václav Studnička²

¹*Department of Electronic Structures, Faculty of Mathematics and Physics, Charles University in Prague, Ke Karlovu 5, 121 16 Praha 2, Czech Republic*

²*Institute of Physics, Academy of Sciences of the Czech Republic, Na Slovance 2, 182 21 Praha 8, Czech Republic*

Texture or, in other words, preferred orientation of grains is one of the most common features of thin layers. Single scans in x-ray diffractometry are always affected by the phenomenon, but usually they are not sufficient to provide any corrections. Any correction introduces more free parameters into the refining process and especially texture corrections provide peak-to-peak different factors, which have to be accounted for in calculation of simulated x-ray diffraction intensities. For simple materials (such as pure metals or perovskites) and using the Cu K α radiation from a Copper anode, there are not many reflections in the whole angle range of diffraction angles. Unfortunately these are the most often used experimental setup and the data are the best for evaluating of some crucial parameters with regard to structure. The only pure way to distinguish the texture effect on intensities from the structural one is to include the texture determination in the process.

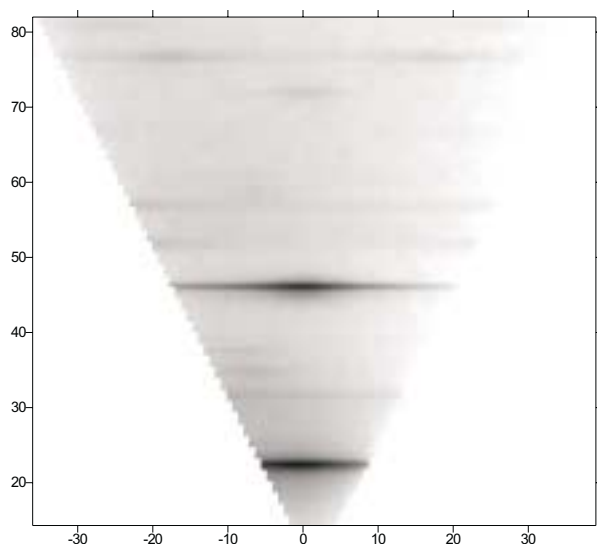


Figure 1a

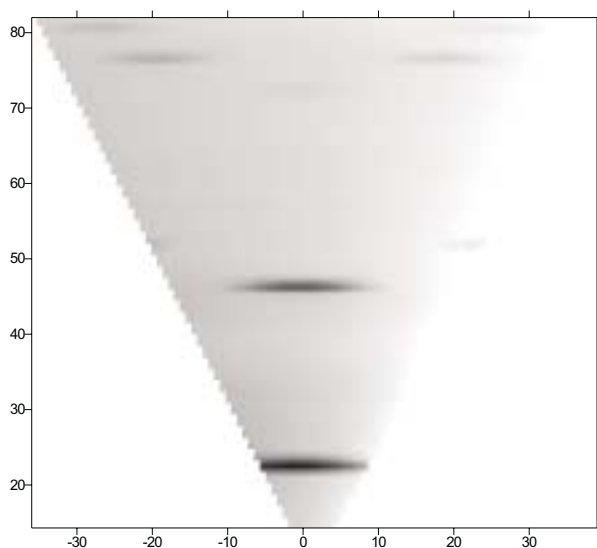


Figure 1b.

Comparison of measured (a) versus calculated (b) intensity map for PbTiO_3 thin layer on glass. Horizontal axis is omega, vertical 2θ angle in degrees. Preferred orientation has the axis perpendicular to the 100 planes, which are preferably oriented perpendicularly to the sample surface. Residual non-textured portion of grain orientation distribution can be observed in the measured data (horizontal lines), which was not accounted for in the simulation.

Strongly textured samples does not show many reflections in a single scan, e.g. the well known $\theta/2\theta$ theta or detector scan with constant GAOI (grazing angle of incidence), thus the texture function is not known in many points. For instance: in symmetric scan on a sample with fibre (rotationally symmetric) texture with its axis perpendicular to the sample surface we know only values of the pole functions corresponding to the reflections preferably oriented parallel and nearly parallel to the texture axis. In order to find out more about them, we have to perform so called omega-scans (or rocking curves) by maintaining constant diffraction angle 2θ . Reflections parallel to the texture axis then have the maximum intensity in the centre, other reflections off the centre of the rocking curve. If we

perform some other ω -scans for different diffraction angles, we also find some other reflections, which were not observed in symmetric scan.

Having made necessary assumptions about the texture (as we did saying it has the rotational symmetry) we can then extend the calculation from a single scan into an ω - 2θ map. There are more reflections in the map than in the single scan and their structure intensities give the evidence about the structure, their 2θ profiles about microstructure and their omega profiles about preferred orientation. One can also observe more complicated ω - 2θ profiles originating from residual strain, which then can be in principal evaluated without knowledge of Poisson ratio. Changes in 2θ profile widths of non-axial reflections with respect to the axial ones then refer about crystallite's shape (discs or needles).

For the sake of the huge variety of sample parameters, which can be extracted from the maps, we decided to develop a component system allowing usage of different models for texture, structure and microstructure to be able to easily obtain the desired parameters. The body of the program consist from a map calculator, which collects information from several components. The components are:

- Instrumental corrections and geometric effects, which correct the misreported angles to the proper ones (e.g. zero shift or eccentricity of sample surface from the goniometer axis in case of Bragg-Brentano geometry), Lorenz and polarisation factor.
- Structure changes, which produces cell parameters (a , b , c , $\cos \alpha$, $\cos \beta$ and $\cos \gamma$) and structure factors F_{HKL} for considered reflections HKL within the previously defined Laue group.
- Profile function, which produces appropriate 2θ profiles as a function of theta and if need be omega. They are dependent on cell parameters and on some other describing broadening and intensity decay (FWHM, Debye-Waller factor, etc.).
- Texture pole functions for several reflections HKL depending on omega.
- Background produced by several layers and phases (depending on diffraction angle)
- Interlayer correlation and attenuation due to absorption, which makes intensity profiles out of the amplitude ones. It determines, whether the lattice of grains in several layers is correlated (in case of multilayers) or not, and also corrects the intensity of deeper layers' reflections for an exponential decay of the x-rays travelling through the matter.

All these components can be chosen separately in accordance with the structure model and with respect to parameters that we need to obtain more or less precisely.

Here we report the first simulations obtained with the testing samples (Fig. 1).

THERMALLY STIMULATED LUMINESCENCE OF SrTiO₃:Mn⁴⁺. MEASURING OF ACTIVATION ENERGIES OF SHALLOW TRAPS.

P. Ptáček, Z. Bryknar, Z. Potůček

Czech Technical University in Prague, Faculty of Nuclear Sciences and Physical Engineering, V Holešovičkách 2, CZ-18000 Praha 8, Czech Republic

1. Introduction

SrTiO₃ is a perovskite paraelectric material, which is, due to high permittivity, in future useful for optoelectronic elements such as memory cells of small dimensions. The SrTiO₃:Mn⁴⁺ has the cubic symmetry above the temperature 105 K. In the center of cube the Ti⁴⁺ ions are situated, in the corners of this cube there are ions of strontium, and the oxygen ions are placed in the centers of the cube sides. At ~105 K it possesses a cubic-tetragonal structural phase transition O^{1_h} → D^{18_{4h}} [1]. The width of forbidden band is 3.26 eV, which was determined by measurements of photocurrents at different temperatures [2]. The band structure was calculated by the LCAO (linear-combination-of-atomic-orbitals) method. Valence band has its origin in 2p orbitals of oxygen and conduction band originates from 3d orbitals of titanium [2]. SrTiO₃:Mn⁴⁺ (10⁻² wt%) single crystals have been grown by the Kyropoulos techniques. The Mn⁴⁺ ions substitute Ti⁴⁺ in octahedral positions. This was inspected by the EPR spectroscopy.

Thermally stimulated luminescence (TSL) is powerful tool for the study of energy levels in the forbidden band. We can say the TSL is the emission of the light during the heating of the sample, but the heating is not the reason of this light emission. The sample must be exposed to a light with appropriate wavelength before heating. After each measurement the levels in the forbidden gap must be totally cleaned up (by the heating), after that the sample must be cooled and again irradiated to fill the levels by the electrons. It is easy to imagine that this measurement is very time difficult.

2. Experimental results and discussion

We have measured the thermally stimulated luminescence of SrTiO₃:Mn⁴⁺ at 12–110 K after light irradiation of the samples from 350–520 nm spectral region. We have observed eleven peaks in the whole TSL spectrum (Fig. 1). It

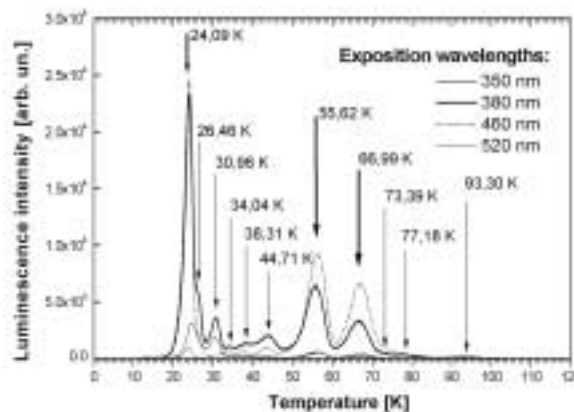


Figure 1. TSL curves of SrTiO₃:Mn⁴⁺ detected at 735 nm. Exposure wavelengths are 350, 380, 460 and 520 nm light of 300 W high pressure xenon lamp. The thick arrows corresponding to bulk levels.

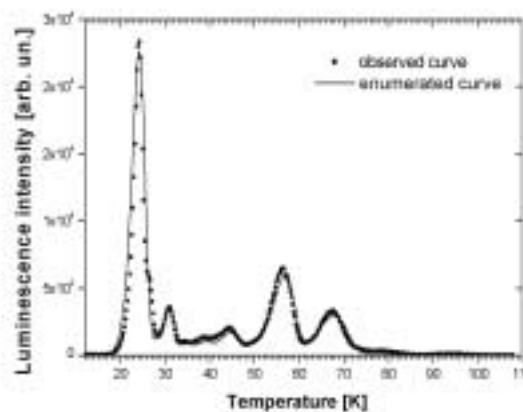


Figure 2. Comparison of the observed and enumerated spectrum of SrTiO₃:Mn⁴⁺. There is a good agreement in the peak positions that determine the activation energies.

was necessary to separate individual peaks for the further analysis of the TSL glow curve. This has been done by partial heating of the sample to the lower temperature than the temperature of the maximum intensity (during this heating we have cleaned up the levels with lower activation energy). After that we have decreased the temperature of the sample. Finally we have measured the given peak (level) during repeated heating [3]. This technique allowed obtaining a smooth leading edge the glow curve peak, which is important for its analysis by “the initial rise method” [4]. The activation energies and corresponding temperatures of

maximum intensity (T_m) are summarized in Table 1. The activation energies were found in the range 33 – 150 meV. How it was mentioned above, the width of forbidden gap of $\text{SrTiO}_3:\text{Mn}^{4+}$ is 3.26 eV so we can speak about really shallow traps in this material.

The separation of the surface states and bulk states is also presented in Fig. 1. The curves for 380 and 460 nm excitation are the good examples of excitation from different spectral regions. The light with wavelength 380 nm has the energy higher than the gap width and it is strongly absorbed in the surface layer, whereas the 460 nm light penetrates into the bulk of the crystal and released electrons fill mainly the bulk levels.

A special computer program was written for comparison purposes of the observed spectrum and the theoretically assumed shape of TSL glow curve. The analytic forms of luminescence intensity were substituted by numerical formulas [4]. The result of this procedure is shown in Fig. 2. There is a good agreement between the observed and calculated spectrum. The most important are the same positions of the peaks in the spectrum, because temperatures of intensity maxima in the TSL spectrum determine the activation energies of given energy levels.

As a detector of the TSL we have used in this work a photomultiplier working in the photo-counting regime. It is very necessary to know also the emission spectra of TSL to determine a nature of recombination centers responsible for the TSL. For this purpose we are preparing a SPH 5 CCD camera (Apogee Instruments Inc.) and we are going to improve the synchronization of the temperature measurement and the emitted intensity. The experiment will be computer controlled by flow-data program in the LabVIEW, which is very powerful tool for it.

Acknowledgements

This work has been supported by the grant of the Czech Grant Agency No.202/00/1425 and by the FR VS grant No.1924/2001.

References :

1. R. A. Serway, W. Berlinger, K. A. Müller, R. W. Collins: *Physical Review B*, 16 (1977), 4761
2. T. Feng: *Physical Review B*, 25 (1982), 627
3. M. Martini, F. Meinardi, G. Spinolo, A. Velda, M. Nikl, Y. Usuki: *Physical Review B*, 60 (1999), 4653
4. R. Chen, Y. Kirsch: *Analysis of Thermally Stimulated Processes*, Pergamon Press (1981)

CRYSTAL AND MOLECULAR STRUCTURES OF BIS(*N,N*-DIETHYLNICOTINAMIDE-*N*)-BIS(2-CHLORONICOTINATE-*O*)-DIAQUACOPPER(II) AND BIS(*N,N*-DIETHYLNICOTINAMIDE-*N*)-BIS(2-CHLOROBENZOATE-*O*)-DIAQUACOPPER(II)

Ján Moncol¹, Marian Koman¹, Milan Melník¹, Tadeusz Glowiak²

¹Department of Inorganic Chemistry, Slovak University of Technology, SK-81237 Bratislava, Slovak Republic, E-mail: moncol@chtf.stuba.sk

²Faculty of Chemistry, Wrocław University, PL-50383, Poland

The molecules of $[\text{Cu}(2\text{-Clnic})_2(\text{Et}_2\text{nia})_2(\text{H}_2\text{O})_2]$ and $[\text{Cu}(2\text{-Clbz})_2(\text{Et}_2\text{nia})_2(\text{H}_2\text{O})_2]$ (2-Clnic = 2-chloronicotinate, 2-Clbz = 2-chlorobenzoate and Et_2nia = *N,N*-diethylnicotinamide) are a crystallographically centrosymmetric mononuclear complexes containing two water molecules, two carboxylate anions (2-chloronicotinate or 2-chlorobenzoate) and two *N,N*-diethylnicotinamide ligands, all ligands acting as monodentate. The copper(II) atoms are bonded in a *trans* square-planar arrangement by two N atoms of two *N,N*-diethylnicotinamide molecules and one carboxylate oxygen atom from each of two 2-chloronicotinate, in the former and 2-chlorobenzoate in the latter. The two water molecules around each copper(II) atom at the axial positions completed a tetragonal-bipyramidal geometry, at the distances of 2.502(2) Å and 2.440(2) Å, respectively.

1. Introduction

The interaction of the Cu(II) atom, which plays a vital role in a number of quite different biological processes [1], with therapeutically administered drugs is a subject of considerable interest. It is known that *N,N*-diethylnicotinamide is an important respiratory stimulant [2].

X-ray analysis some copper(II) carboxylates with *N,N*-diethylnicotinamide show that are binuclear [2-4] with tetracarboxylate bridge between two Cu(II) atoms, mononuclear with unidentate [5-7] or bidentate [7, 9] bonded carboxylate anions or polynuclear structure [10]. The present paper describes crystal and molecular structures of $[\text{Cu}(2\text{-Clnic})_2(\text{Et}_2\text{nia})_2(\text{H}_2\text{O})_2]$ and $[\text{Cu}(2\text{-Clbz})_2(\text{Et}_2\text{nia})_2(\text{H}_2\text{O})_2]$ (2-Clnic = 2-chloronicotinate, 2-Clbz = 2-chlorobenzoate and Et_2nia = *N,N*-diethylnicotinamide).

2. Experimental

2.1. Preparation

Preparation of $[\text{Cu}(2\text{-Clnic})_2(\text{Et}_2\text{nia})_2(\text{H}_2\text{O})_2]$

The copper(II) 2-chloronicotinate monohydrate was prepared as described by Moncol *et al.* [11]. The light blue

crystals of $[\text{Cu}(2\text{-Clnic})_2(\text{Et}_2\text{nia})_2(\text{H}_2\text{O})_2]$ were prepared by mixing of a methanol solution of copper(II) 2-chloronicotinate monohydrate with a *N,N*-diethylnicotinamide at the molar ratio of 1:2. The solution was left to stand at room temperature and blue microcrystals precipitated, were filtered off. The blue crude product was recrystallized from methanol.

Preparation of $[\text{Cu}(2\text{-Clbz})_2(\text{Et}_2\text{nia})_2(\text{H}_2\text{O})_2]$

The copper(II) 2-chlorobenzoate monohydrate was prepared as described by Kawata *et al.* [12]. The dark blue crystals of $[\text{Cu}(2\text{-Clbz})_2(\text{Et}_2\text{nia})_2(\text{H}_2\text{O})_2]$ were prepared by mixing of a methanol-acetone (2:1) solution of copper(II) 2-chlorobenzoate monohydrate with a of *N,N*-diethylnicotinamide at the molar ratio of 1:2. The solution was left to stand at room temperature and the green microcrystals precipitated, were filtered off. The filtrate was left to stand at room temperature and blue microcrystals precipitated, were filtered off. The blue crude product was recrystallized from acetone.

2.1 X-ray analysis

Data collection and cell refinement for $[\text{Cu}(2\text{-Clnic})_2(\text{Et}_2\text{nia})_2(\text{H}_2\text{O})_2]$ were carried out using KUMA KM4CCD diffractometer software [13a] at 293 K. The diffraction intensities were corrected for Lorentz and polarization factors. The structure was solved by Heavy atom methods using SHELXS86 [14]. Geometrical analysis was performed using SHELXL93 [15]. The structures of the complexes were drawn by ORTEP-III [16] (Fig. 1.). The light blue $[\text{Cu}(2\text{-Clnic})_2(\text{Et}_2\text{nia})_2(\text{H}_2\text{O})_2]$ crystallizes in triclinic system, space group *P*-1 (No. 2) with unit cell parameters: $a = 7.174(1) \text{ \AA}$, $b = 8.705(2) \text{ \AA}$, $c = 14.329(3) \text{ \AA}$, $\alpha = 97.02(3)^\circ$, $\beta = 97.47(3)^\circ$, $\gamma = 103.89(3)^\circ$ and $Z = 1$. The cell parameters were refined in the range 2.90 to 29.03° . 5846 reflections in total were refined, index range $-9 \leq h \leq 7$, $-11 \leq k \leq 11$, $-19 \leq l \leq 19$. Independent reflections were 3768 ($R_{\text{int}} = 0.0285$). Goodness-of-fit, S , was 1.194. The final values were $R = 0.0614$ and $R_w = 0.1541$.

Data collection and cell refinement for $[\text{Cu}(2\text{-Clbz})_2(\text{Et}_2\text{nia})_2(\text{H}_2\text{O})_2]$ were carried out using KUMA KM4CCD diffractometer software [13b] at 100 K using an Oxford Cryosystems cooler device [16]. The diffraction intensities were corrected for Lorentz and polarization factors. The structure was solved by Direct methods using SHELXS97 [17]. Geometrical analysis was performed using SHELXL97 [18]. The structures of the complexes were drawn by ORTEP-III [15] (Fig. 2.). The dark blue $[\text{Cu}(2\text{-Clbz})_2(\text{Et}_2\text{nia})_2(\text{H}_2\text{O})_2]$ crystallizes in monoclinic system, space group $P2_1/n$ (No. 14) with unit cell parameters: $a = 12.354(2) \text{ \AA}$, $b = 10.689(2) \text{ \AA}$, $c = 14.730(3) \text{ \AA}$, $\beta = 112.94(3)^\circ$ and $Z = 2$. The cell parameters were refined in the range 3.35 to 28.62° . 12380 reflections in total were refined, index range $-16 \leq h \leq 15$, $-14 \leq k \leq 13$, $-19 \leq l \leq 19$. Independent reflections were 4290 ($R_{\text{int}} = 0.0394$). Goodness-of-fit, S , was 1.082. The final values were $R = 0.0415$ and $R_w = 0.0965$.

3. Results and Discussion

The principal structural features of $[\text{Cu}(2\text{-Clnic})_2(\text{Et}_2\text{nia})_2(\text{H}_2\text{O})_2]$ is illustrated in Fig. 1. The coordination environment of the copper(II) atom is tetragonal bipyramidal. The tetragonal plane is built up by a pair of unidentate 2-chloronicotinate anions by carboxylate oxygen atoms [$\text{Cu}-\text{O}(1) = 1.966(2) \text{ \AA}$] and by a pair of neutral *N,N*-diethylnicotinamide molecules using pyridine ring nitrogen atoms [$\text{Cu}-\text{N}(1) = 2.015(2) \text{ \AA}$] in *trans* positions. The axial positions are occupied by water molecules [$\text{Cu}-\text{O}(1\text{W}) = 2.502(2) \text{ \AA}$]. The carbonyl oxygen atom of carboxylic group is disordered occupying two statistical positions, represented by O(2A) and O(2B) with the site occupying factors of 0.44(7) and 0.56(7), respectively. There are intermolecular hydrogen bonds ($\text{O}\dots\text{H}\dots\text{O}$) between water oxygen atom and disordered carboxyl oxygen ($\text{O}(1\text{W})\dots\text{O}(2\text{A})$ and $\text{O}(1\text{W})\dots\text{O}(2\text{B})$) at distances 2.652(9) and 2.736(8) \AA , respectively. Distance $\text{O}(1\text{W})\dots\text{O}(3\text{b})$ [$-x+1, -y+1, -z$] is 2.850(3) \AA , which is typical values for $\text{O}\dots\text{H}\dots\text{O}$ intramolecular hydrogen bonded system.

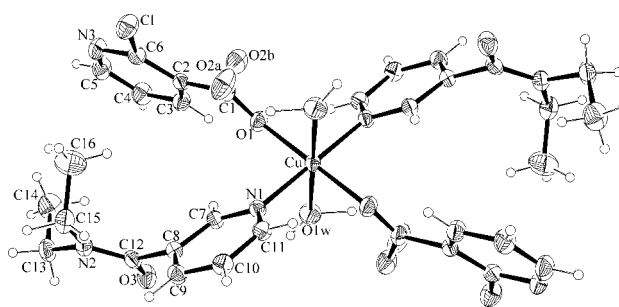


Figure 1. Perspective view of complex $[\text{Cu}(2\text{-Clnic})_2(\text{Et}_2\text{nia})_2(\text{H}_2\text{O})_2]$, with the atom numbering scheme. Thermal ellipsoids are drawn at the 30% probability level.

The structure of $[\text{Cu}(2\text{-Clbz})_2(\text{Et}_2\text{nia})_2(\text{H}_2\text{O})_2]$ is shown in Fig. 2 together with the atomic numbering. The geometry around the copper(II) atom is tetragonal bipyramidal with equatorial plane formed by a pair of unidentate 2-chloronicotinate anions using carboxylate oxygen atoms [$\text{Cu}-\text{O}(1) = 1.958(1) \text{ \AA}$] and by a pair of neutral *N,N*-diethylnicotinamide molecules using pyridine ring nitrogen atoms [$\text{Cu}-\text{N}(1) = 2.031(2) \text{ \AA}$] in *trans* positions. The two apical positions are formed by the two oxygen atom of water molecule with a distances of $\text{Cu}-\text{O}(1\text{W}) = 2.440(2) \text{ \AA}$. The benzene ring of 2-chlorobenzoate anions is disordered. The two statistical positions of chlorine atoms are represented by Cl(1) and Cl(2) with the site occupying factors of 0.15(1) and 0.85(1), respectively. A hydrogen bond systems ($\text{O}\dots\text{H}\dots\text{O}$) are present between water oxygen atom and carbonyl oxygen atom of *N,N*-diethylnicotinamide $\text{O}(1\text{W})\dots\text{O}(2\text{b})$ [$+x+1/2, -y+1/2, -z+1$], and between water oxygen atom and carboxyl oxygen atom $\text{O}(1\text{W})\dots\text{O}(2\text{c})$ [$-x, -y, -z+1$], with $\text{O}\dots\text{O}$ distances of 2.808(2) and 2.713(2) \AA , respectively, causing a weak intramolecular interactions.

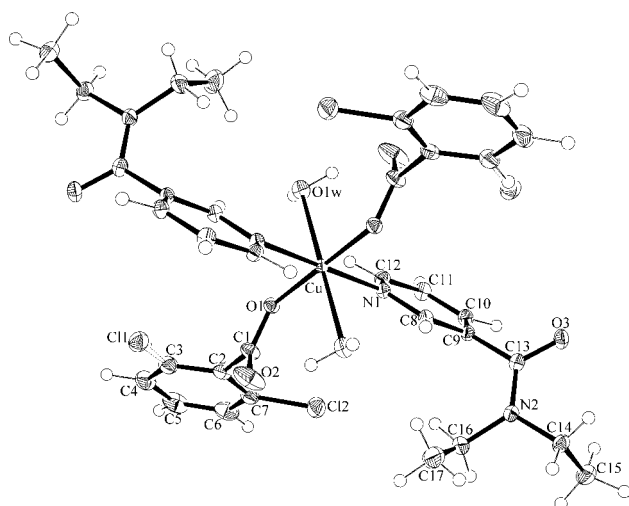


Figure 2. Perspective view of complex $[\text{Cu}(\text{2-Clbz})_2(\text{Et}_2\text{nia})_2(\text{H}_2\text{O})_2]$, with the atom numbering scheme. Thermal ellipsoids are drawn at the 50% probability level.

References

1. D. Kovala-Demertzi, A. Theodorou, M.A. Demertzis, C.P. Raptopoulou, A. Terzis, *J. Inorg. Biochem.* **65** (1997) 151.
2. T. Hökelek, H. Necefoglu, M. Balci, *Acta Cryst.*, **C51** (1995) 2020.
3. L. Kh. Minacheva, T.S. Khodashova, M.A. Porai-Koshits, A.Yu. Tsivadze, *Koord. Khim.*, **7** (1981) 455.
4. B. Kozlevčar, N. Lah, I. Leban, F. Pohleven, P. Šegedin, *Croat. Chim. Acta*, **73** (2000) 733.
5. M. Melník, I. Potočan, E. Macáškova, D. Mikloš, C.E. Holloway, *Polyhedron*, **15** (1996) 2159.
6. T. Hökelek, K. Budak, H. Necefoglu, *Acta Cryst.*, **C53** (1997) 1049.
7. M. Melník, M. Koman, E. Macáškova, T. Glowiak, *J. Coord. Chem.*, **44** (1998) 163.
8. T. Hökelek, H. Gündüz, H. Necefoglu, *Acta Cryst.*, **C52** (1996) 2470.
9. M. Koman, M. Melník, T. Glowiak, *J. Coord. Chem.*, **44** (1998) 133.
10. F. Valach, M. Dunaj-Jurčo, M. Melník, N.N. Hoang, *Z. Kristallogr.*, **209** (1994) 267.
11. J. Moncol, P. Segla, M. Koman, M. Korabik, M. Melník, T. Glowiak, J. Mrozinski, *Inorg. Chim. Acta*, submitted for publication.
12. T. Kawata, S. Ohba, T. Tokii, Y. Muto, M. Kato, *Acta Cryst.*, **C48** (1992) 1590.
13. (a) KUMA, KM4SYS. (Program for Data Reduction for KM4CCD Version 1.149), Wrocław, Poland (1998); (b) KUMA, CRYALIS. (Program for Data Reduction for KM4CCD Version 1.166), Wrocław, Poland (2000).
14. G.M. Sheldrick, SHELXS86. (Crystallographic Computing 3, G.M. Sheldrick, C. Krueger, R. Goddard) 175-189. Oxford Univ. Press (1985).
15. G.M. Sheldrick, SHELXL93. (Program for Refinement of Crystal Structure). Univ. Göttingen, Germany (1994).
16. (a) M.N. Burnet, C.K. Johnson, ORTEP-III. (Oak Ridge Thermal Ellipsoid Plot Program for Crystal Structure Illustration). Report ORNL-3895. Oak Ridge National Laboratory, Tennessee (1996); (b) L.J. Farrugia, *J. Appl. Cryst.*, **30** (1997) 568.
17. J. Cosier, A.M. Glazer, *J. Appl. Cryst.*, **19** (1986) 105.
18. G.M. Sheldrick, *Acta Cryst.*, **A46** (1990) 467.
19. G.M. Sheldrick, SHELXL97. (Program for the Solution and Refinement of Crystal Structures). Univ. Göttingen, Germany (1997).

STUDIES OF COMPLEXATION PROPERTIES OF CALIXARENE DERIVATIVES

Jan Sýkora

Department of Solid State Chemistry, Prague Institute of Chemical Technology, Technická 5, 166 28 Prague 6, Czech Republic; e-mail: jan.sykora@vscht.cz

The shape of calixarene molecule is suitable for formation of various complexes. Substitution of the calixarene unit allows the complexation of ions and also of neutral molecules [1]. At the present time many crystallographic structures of calixarenes with molecule of solvent inside the cavity are available [2]. The usual complexation ratio is 1:1. However, there are several cases where the solvent molecule forms complexes with two calixarene units. The typical examples are complexes of p-tert-butylcalix[4]arene with toluene (1:1) [3] or anisole (2:1) [4].

Recently discovered approach of isolation of pure fullerene C_{60} is another example of possible complexation of neutral molecule [5]. The process of separation consists of diluting of raw mixture of fullerenes in toluene solution of p-tert-butylcalix[8]arene. The complex of p-tert-butylcalix[8]arene with C_{60} in ratio 1:2 is preferred under these conditions. Driving force of that complexation is a forming of hydrogen bonds and π -interaction. The shape of the cavity predetermines calixarenes to complex cations. There are many derivatives with selective complexation properties towards the alkali metals, alkali earth metals, transuranium metals etc. For example tetraester derivatives complex univalent cations. Trapped cation is surrounded by four phenolic and four ester oxygen atoms [6]. The higher selectivity towards the particular alkali metals has been achieved by attaching ethylenglycolic units to phenolic oxygen atoms. Calix[4] crownethers prepared this way show the highest selectivity towards the Na^+ or K^+ ions depending on number of ethylenglycolic units [7]. It's inevitable to add electron accepting groups to lower or upper rim for complexation of anions. Addition of amide groups leads to the cavity suitable for anion trapping (Fig. 1). These complexes are stable due to simultaneous effect of hydrogen bonds and electrostatic forces [1]. The substitution of methylene bridges by sulfur atoms is another case how to modify complexation properties. It leads to the increase of the cavity size. Modified molecules create complexes with larger solvent molecules than its classical analog. We can also take advantage of the oxidation of the sulfur atoms yielding to various sulfoxides and sulfones

[8]. Complexed molecule occurs mostly at the vertical axis of the cavity [2]. The atoms are very often disordered to several positions. The number of positions is often equal to the number of aromatic rings presented in the calixarene. In this case disordered atoms have the same occupancy factors (Fig. 2).

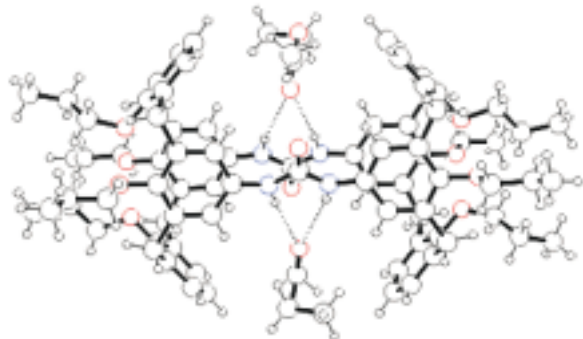


Figure 1. Crystal structure of double urea bridged bis-calix[4]arene. This compound shows an interesting complexation properties towards anions. It's stabilized by two molecules of ethylacetate in the solid state.

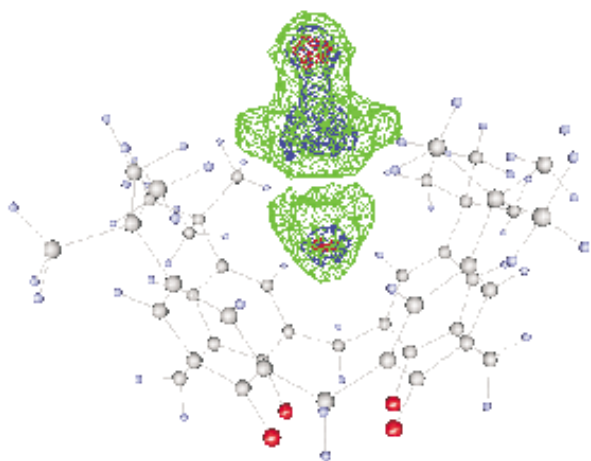


Figure 2. Difference electron density map of p-tert-butylcalix[4]arene with molecule of ethylacetate inside the cavity.

This work was supported by the Ministry of Education, Youth and Sports of the Czech Republic (research project No. CEZ:MSM 223100002). Searching in database CSD was enabled on the basis of the grant of GA ČR 203/99/0067.

1. C.D. Gutsche: Calixarenes: Monographs in Supramolecular Chemistry Vol. 1, The Royal Society of Chemistry, Cambridge 1989 (J. F. Stoddart, Ed.).
2. Cambridge Structure Database.
3. A. Arduini, R. Caciuffo, S. Geremia, C. Ferrero, F. Ugozzoli, F. Zontone, *Supramolecular Chemistry*, **10** (1998), 125.
4. R. Ungaro, A. Pochini, G.D. Andreotti, P. Domiano, *J. Chem. Soc., Perkin Trans. 2*, (1985), 197.
5. J.L. Atwood, L.J. Barbour, C.L. Raston, I.B.N. Sudria, *Angew. Chem., Int. Ed. Engl.*, **37** (1998), 981.
6. A. Ikeda, S. Shinkai, *Chem. Rev.*, **97** (1997), 1713.

7. F. Ugozzoli, O. Ori, A. Casnati, A. Pochini, R. Ungaro, D.N. Reinhoudt, *Supramolecular Chemistry*, **5** (1985), 179.
8. H. Kumagai, M. Hasegawa, S. Miyanari, Y. Sugawa, Y. Sato, T. Hori, S. Ueda, H. Kamiyama, S. Miyano, *Tetrahedron Letters*, **38** (1997), 3971.

AN INFLUENCE OF SYNTHESIS ON STRUCTURAL PROPERTIES OF α -Fe₂O₃

Jan Walla¹, Dagmar Krausová¹,
Radek Zbořil¹, Miroslav Mašlán²

¹Department of Inorganic Chemistry, Palacky University, 772 47 Olomouc, Czech Republic

²Department of Experimental Physics, Palacky University, 772 47 Olomouc, Czech Republic

Iron(III) oxide, Fe₂O₃, belongs to the most important inorganic compounds. Its most common form occurring in nature is hexagonal α -Fe₂O₃, hematite, which is used as a raw material for iron production. Apart from this it is capable of forming another metastable crystalline modifications, such as cubic β and γ or orthorhombic ϵ modifications.

The most usual modification, hematite, or α -Fe₂O₃, has unusually interesting magnetic characteristics emerging from its structure; this offers its utilisation in production of tapes, discs etc. It is also widely used as a stable red pigment.

Hematite has rhombohedrally centered hexagonal structure of the corundum type with closed oxygen lattice, where two thirds of octahedral positions are occupied by Fe³⁺ ions. The iron atoms are surrounded with six oxygen atoms in a shape of deformed octahedron. That shares one of its walls with one adjacent octahedron and three edges with three adjacent octahedrons. Thus there are two different bonds Fe—O and two different, relatively small distances between the adjacent iron atoms, which is a reason for its very interesting magnetic properties.

α -Fe₂O₃ as a red pigment is produced by two methods basically. It is:

- I - "dry method", the principle of which is a gradual thermal conversion (calcination) of Fe₂SO₄·7H₂O at temperatures 600-800°C, and
- II - "wet method", the principle of which is a reaction of ferrous salt with reducible aromatic nitro-compound (nitro- or azoderivatives) and a base under higher temperatures (about 25-200°C) in an aqueous medium.

The aim of the present work was to find the influence of synthesis or another factors on structural properties and also on the colour quality of these pigments. Four samples of industrially made pigments were analysed, two of them prepared by calcination - "dry" method (samples IA and IB), two were prepared by the "wet" method (samples IIA and IIB).

The samples were studied with physico-chemical methods to find the impact of preparative method on structural characteristics. XRD patterns were obtained with a XRD-7 device, basic crystallographic data were then refined by Rietveld method (Tab. 1).

Table 1. Basic crystallographic data

Sample	IA	IB	IIA	IIB
Space group	$R\bar{3}c$	$R\bar{3}c$	$R\bar{3}c$	$R\bar{3}c$
A=b (Å)	5.0231(1)	5.02488(7)	5.03147(7)	5.02986(8)
c (Å)	13.7166(2)	13.7221(2)	13.7405(2)	13.7362(2)
Fe z/c (00z)	0.3554(7)	0.3552(7)	0.3552(8)	0.3552(7)
O x/a (x0¼)	0.3062(7)	0.3061(7)	0.3072(8)	0.3071(7)
R _p	7.43	8.14	7.69	7.43
R _{wp}	12.02	12.73	11.95	11.49

Table 2. Bond lengths and IR data

	IA	IB	IIA	IIB
Fe-O1 (Å)	1.937	1.939	1.940	1.937
Fe-O2 (Å)	2.112	2.111	2.116	2.119
ν_1 (cm ⁻¹)	548	550	577	581
ν_2 (cm ⁻¹)	475	475	481	481

A significant decrease of lattice parameters was observed in samples prepared by calcination.

The results of IR spectroscopy proving the existence of two unequal bonds Fe—O, are in compliance with the above-mentioned finding (Tab. 2).

Mössbauer spectra at room temperature were also measured. Only sextet Fe³⁺ was always identified with parameters of isomer shift IS=0.37 mm/s, quadrupole splitting QS=-0.21 mm/s and magnetic splitting B~51T. Samples *I* show lower values B (50.8 comparing to 51.3), most likely as an impact of varying structural parameters.

The samples were further investigated in terms of impurities by the method of X-ray fluorescence analysis, primarily in terms of possible cation substitution. In all the cases the hematite contained only small contents of impurities, the samples *IA* and *IB* were found to contain an increased contents of S and Ti (about 1%), most likely as a heterogeneous impurities from raw material. Samples *I* were found to contain small portions of Mg and Mn as possible cation substituents, samples *II* then Mn, Cr, and Al, however, always in a very low concentrations (up to 0.1%), which cannot have a significant impact on structural parameters.

It is well known that iron oxides are the oldest-known colorants, chemically stable, non-toxic, non-bleeding and highly durable with excellent suspension properties. α -Fe₂O₃ (hematite) is the most frequent red inorganic pigment with a very high heat resistance as a superior pigmentary property. In the present comparative study two types of α -Fe₂O₃ samples have been prepared by non-equivalent ways. "Dry" way of α -Fe₂O₃ synthesis was based on the thermal decomposition of FeSO₄·7H₂O in the air. The synthesis includes several stages: the partial dehydration of ferrous sulfate heptahydrate to monohydrate at 200 °C, the milling and sorting of particles, calcination at temperatures 600-800 °C, dissolution of possible sulfato-intermediates in the water, filtration and drying of the final pigment. The size of α -Fe₂O₃ particles can be varied depending on the calcination temperature and the used sort of the initial particles. When using "wet" way, iron oxide pigment was produced by reacting a ferrous salt, a reducible aromatic nitrocompound (nitro- or azoderivates) and a basic compound, chosen from hydroxides of ammonium and

THE INFLUENCE OF SYNTHESIS ON THE SIZE AND MORPHOLOGY OF α -Fe₂O₃ PARTICLES

M. Vůjtek¹, R. Zbořil², M. Mašlák¹ and P. Pikal³

¹Department of Experimental Physics, Palacky University, 771 46 Olomouc, Czech Republic

²Department of Inorganic and Physical Chemistry, Palacky University, 771 47 Olomouc, Czech Republic

³Research Department, PRECHEZA, 750 62 Prerov, Czech Republic

Iron oxides are very important materials in several fields of industry and science. They are used as catalysts, pigments, gas sensors, abrasives, polishing agents or magnetic recording media. Iron oxides are the basis for magnetic prospecting of archeological areas as well as for the production of iron or ferrites.

Table 1. Results of DLS analysis

Sample	Mean diameter [nm]	Half width [nm]	Asymmetry parameter
I/A	278	122	0.507
I/B	247	122	0.480
I/C	250	111	0.486
I/D	371	160	0.509
I/E	251	102	0.526
II/A	300	120	0.541
II/B	377	140	0.539
II/C	261	86	0.538
II/D	319	105	0.573
II/E	318	125	0.570

Samples I were prepared by dry way

Samples II were prepared by wet way

alkali metals, operating at 25-200 °C, in an aqueous medium. The size (and colour) of pigment particles can be varied by increasing the reaction temperature and the molar ratio between ferrous salt and aromatic nitrogen compound.

The way of synthesis can influence not only an internal structure of α -Fe₂O₃ but also they can modify the morphology of particles and their size distribution. Just the influence of the method of synthesis on external pigment characteristics and consequently on the pigment colour quality was studied and discussed in the present work.

Samples were characterized by dynamic light scattering method - DLS (particle size distribution), non-contact atomic force microscopy - AFM (the morphology of particles) and the elastic scattering visible spectroscopy (the colour quality of pigments).

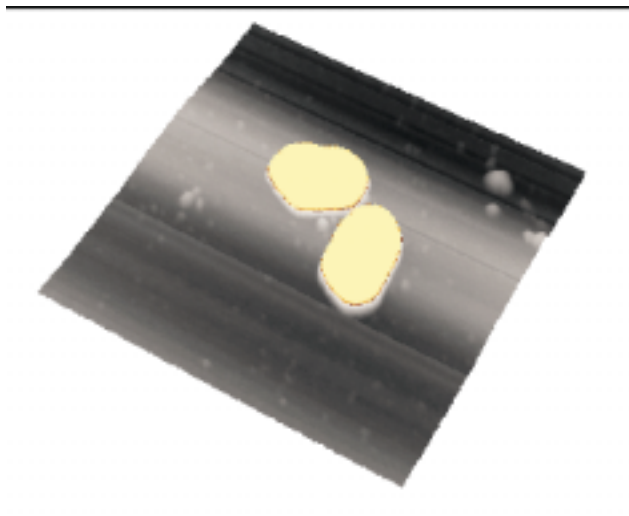


Figure 1. AFM image of α -Fe₂O₃ particles prepared by wet way, section in xy plane (scan size: 680 x 680 nm)

Concerning the general description of particles morphology using AFM measurements, all observed particles showed the symmetrical shape like “flat hexagonal scales” (Figure 1) - lateral dimensions were about 10-30 times greater than the vertical dimension, independently on the type of pigment. However particles of α -Fe₂O₃ prepared by dry way showed about 3 times greater the vertical dimension than the crystallites prepared by the wet way, at comparable lateral dimensions.

Particle size distributions were measured using DLS method, experimental data were approximated by log-normal fit from which three basic characteristics – a mean diameter, a half width of distribution curve and an asymmetry parameter - were calculated (see Table 1). Results summarized in table 1 indicate that the asymmetry parameters are significantly higher for samples prepared by wet way (average value 0.550 vs. 0.500). Values of mean diameters are dependent not only on the method of pigment synthesis (dry vs. wet) but also on the specific conditions during preparation (reaction temperature). Nevertheless it is evident that samples prepared by wet way show higher values of mean diameters though the half width distribution values are almost the same.

To assess the colour quality of pigments the elastic scattering visible spectra were measured in the wavelength range of 400-750 nm. The results of these measurements for both sets of pigments are presented in the standard form of two-dimensional colour co-ordinates (Figure 2). Two mutually perpendicular directions can be highlighted. The first direction marks changes in the colour quality produced by different values of mean diameters, the second direction corresponds to the shift due to the different asymmetry parameters.

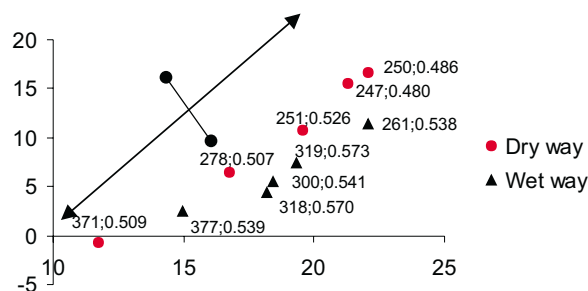


Figure 2. The colour co-ordinates of α -Fe₂O₃ samples and directions of influence of mean diameter (arrow) and asymmetry parameter (line with disks)

KNOWN-UNKNOWN STRUCTURE OF CASSITERITE

M. Klementová

Department of Geochemistry, Mineralogy and Mineral Resources, Faculty of Science, Charles University, 128 43 Praha, Czech Republic

Cassiterite, SnO₂, belongs to the rutile structural group whose members crystallize in space group P4₂/mnm. Cell parameters of synthetic SnO₂ are: $a = 4.7358 \text{ \AA}$, $c = 3.1851 \text{ \AA}$ at 295°K [1]. According to [2], there are two types of coordination octahedra in the structure of cassiterite. One is occupied by Sn and the other is vacant. Only during heterovalent substitutions, excess Fe³⁺ may enter this position. In order to elucidate substitution mechanisms, the structure of cassiterite was studied thoroughly by means of coordination maps based on the effective coordination numbers (EcoN) [3].

Instead of the “vacant” octahedron, there are in fact two tetrahedral positions (d, i) in the structure of cassiterite. These positions can be occupied by ions with radius cca 0.5 Å such as Fe³⁺, Mo⁶⁺, Nb⁵⁺, Ta⁵⁺, Ti⁴⁺, W⁶⁺ and U⁶⁺. In addition to positions d, i , there is another one (g) that has the same number of sites as position containing O. However, because the tetrahedron of position g shares a face with the Sn-octahedron, it is unlikely to be occupied.

The possible structural positions in cassiterite shown in Table 1.

Table 1. The possible structural positions in cassiterite are:

polyhedron	ion	number of sites	Wyckoff notation	point symmetry	position	x	y	z
octahedron	Sn	2	a	mmm	0, 0, 0	0	0	0
tetrahedron	T	4	d	$\bar{4}$	0, 1/2, 1/4	0	1/2	1/4
tetrahedron	O	4	f	mm	x, x, 0	0.3071	0.3071	0
tetrahedron	T	4	g	mm	x, \bar{x} , 0	0.3071	-0.3071	0
tetrahedron	T	8	i	m	x, y, 0	0.1018	0.6333	0

1. H. Seki, N. Ishizawa, N. Mizutani & M. Kato, *YGKSA (J. Cer. Assoc. Japan)*, **92** (1984) 219-223.
2. L. Izoret, G. Marnier & Y. Dasausoy, *Can. Mineral*, **23** (1985) 221-231.
3. R. Hoppe, *Zeits. Krist.*, **150** (1979) 23-52.

INTERCALATION OF ORGANIC MOLECULES INTO PHYLLOSILICATES AND TaS₂

M. Pospíšil and P. Čapková

Department of Chemical Physics and Optics, Faculty of Mathematics and Physics, Charles University Prague, Ke Karlovu 3, 12116 Praha 2, Czech Republic

Organically modified clays are of great technological interest because of their applications in many fields of material research, industry and environmental issues. They are potentially useful as catalysts, sorbent, molecular sieves, fillers to polymer matrix etc [1-3]. Modification of layered structures such as phyllosilicates or TaS₂ by organic species can be achieved by two different ways:

- Ion-exchange interactions based on exchange of interlayer exchangeable cations by organoammonium cations
- Adsorption of polar organic molecules based on ion-dipole interactions with interlayer cations and host layers

Structure analysis of these intercalates is extremely difficult due to their disorder, especially in the interlayer space, but the knowledge of structure is need to understanding of the physical and chemical properties of intercalated layered structures.

In present we investigated the structures of montmorillonite intercalated with cetyltrimethylammonium and cetylpyridinium cations, with non-polar molecules of octadecylamine and structure TaS₂ intercalated with cations of methylene blue using molecular mechanics and molecular dynamics simulations combined with infrared spectroscopy and X-ray powder diffraction. As a result of this complex structure analysis we obtain the detailed structure model including the characterization of disorder, the charge distribution and the energy characteristics such as total sublimation energy, partial host-guest and guest-guest interaction energies, exfoliation energy and

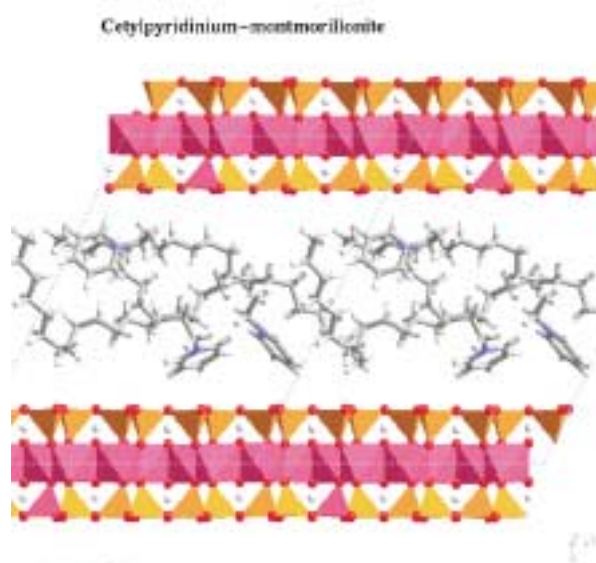


Figure 1. The side view of the structure cetylpyridinium-montmorillonite with 3 pyridinium molecules in $2a \times 2b \times 1c$ supercell (two supercells are visualized in projection along a direction).

their Van der Waals and Coulomb components. Molecular simulations were carried out in a Cerius² modelling environment [4].

Results for montmorillonite intercalated with cetylpyridinium (Fig. 1) and cetyltrimethylammonium (Fig. 2) cations showed that the structures of both intercalates exhibit two main common features: disordered monolayer arrangement of alkyl chains and no regular positions and orientations of pyridinium and ammonium head groups with respect to silicate layers. The head groups for ammonium and pyridinium reside in the upper and lower margins of monolayer in interlayer space of montmorillonite. On the other hand the charge distribution in both intercalates was different. In the case of cetyltrimethylammonium-montmorillonite the total charge of silicate layers per one supercell ($2a \times 2b \times 1c$) is negative. That is the usual behavior of smectites intercalated with organo-ammonium cations. In contrast of this the total charge of silicate layer per one supercell in the case of cetylpyridinium-montmorillonite is positive. The charge of silicate layers depend on charge transfer between interlayer cations and layers and in case of cetylpyridinium cations is lower than in case cetyltrimethylammonium cations. The result of this is lower host-guest electrostatic interactions and also lower total

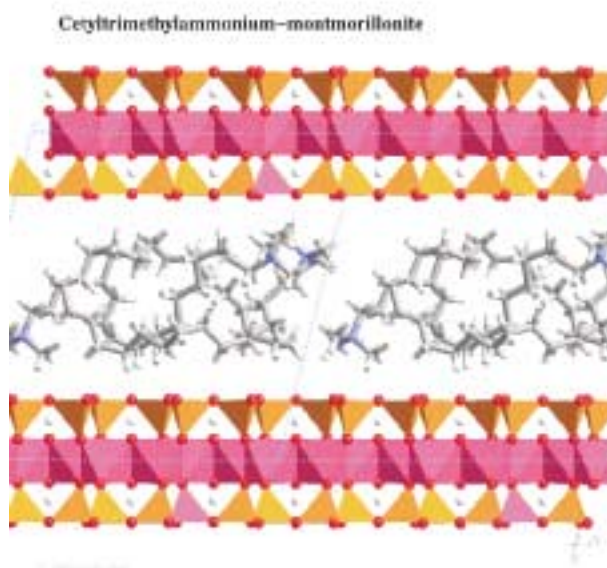


Figure 2. The side view of the structure cetyltrimethylammonium-montmorillonite with 3 cetyltrimethylammonium molecules in $2a \times 2b \times 1c$ supercell (two supercells are visualized in projection along a direction).

host-guest and total sublimation energy in sample of cetylpyridinium-montmorillonite [5].

The investigation of octadecylamine intercalated in montmorillonite based on the ion-dipole interaction (Fig. 3) was the first step in polymer clay nanocomposite technology. The interlayer structure and exfoliation energy exhibits the strong dependence on the octadecylamine concentration. Moreover, the mutual interaction of host layers, Na^+ -cations and octadecylamine molecules leads to unusual distribution of charge in investigated structures.

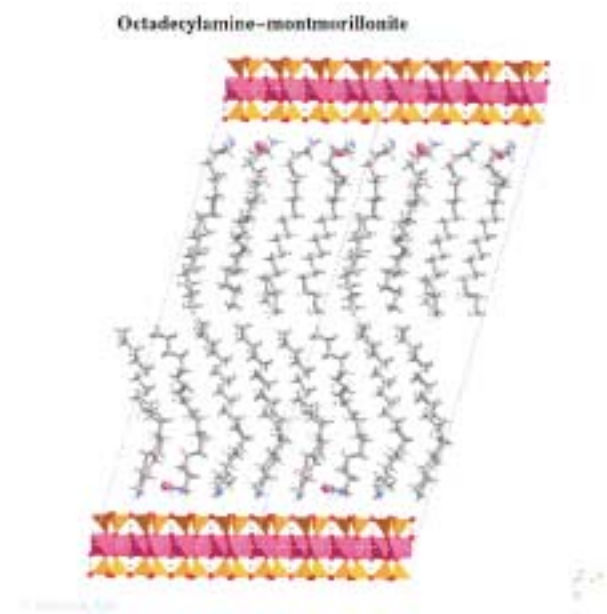


Figure 3. The side view of the structure octadecylamine-montmorillonite with 16 octadecylamine molecules in $2a \times 2b \times 1c$ supercell (two supercells are visualized in projection along a direction).

The charge of silicate layers is positive for higher concentration of octadecylamine molecules. The values of exfoliation energy show that exfoliation of silicate layers is easier for bilayer than for monolayer arrangement of octadecylamine molecules in interlayer space of silicates. These results confirm possible using Na-montmorillonite intercalated with octadecylamine molecules as a precursor for clay/polymer nanocomposite.

Structure analysis of 2H-TaS_2 intercalated with Methylene Blue (MB) included investigation of three different phases with different concentration of Methylene Blue cations. Phase I-MB-TaS₂ – 1 cation of methylene blue in interlayer space (Fig. 4), phase II-MB-TaS₂ – 2 cations of methylene blue, phase III-MB-TaS₂ – 3 cations of methylene blue. The charge distribution depends on guest concentration. Higher concentration of guest leads to higher concentration layer charge and charge transfer during preparation is mainly used for the charge reduction MB cations. The calculated total sublimation energy for I phase is higher than for other phases and this show that I phase is the most stable one. This result is also confirmed experimentally. The calculated and experimental basal spacings are in a good agreement for I phase and III phase. The II phase is not pure phase, but interstratified mixture I phase and II phase and this may be explained by Hendricks-Teller effect [6].

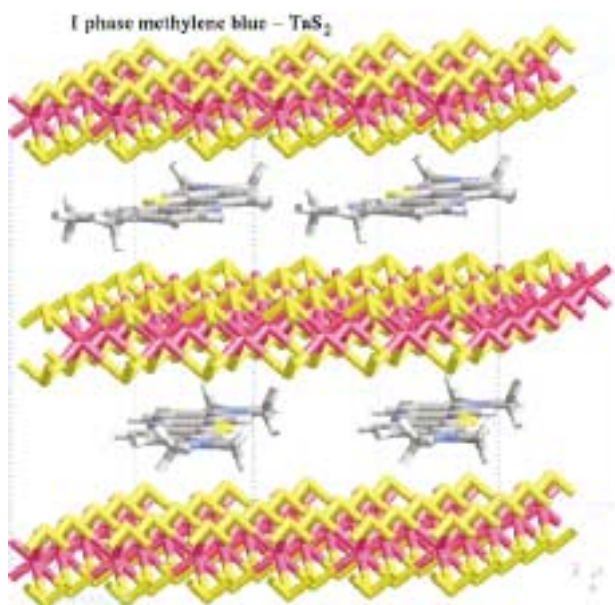


Figure 4. The side view of the structure I phase methylene blue-TaS₂ with 2 methylene blue molecules in $3a \times 5b \times 1c$ supercell (two supercells are visualized in projection along b direction).

References

1. G. Lagaly, *Solid State Ionics*, 22 (1986) 43.
2. P. Čapková, M. Pospíšil, J. Miché-Brendlé, M. Trchová, Z. Weiss & R. Le Dred, *J. Mol. Model*, 6 (2000) 600

3. G. W. Beall & S. J. Tshipurski: Nanocomposites Produced Utilizing a Novel Ion-Dipole Clay Surface Modification. Nanocor Inc., Arlington Heights, IL, 1998.
4. "Cerius² User Guide." Molecular Simulations Inc., San Diego, 1997.
5. M. Pospíšil, P. Čapková, D. Měřínská, Z. Maláč & J. Šimoník, *J. Colloids Interface Sci.*, 236 (2001) 127.
6. S. Hendricks, E. Teller, *J. Chem. Phys.*, 10 (1942) 147.

SUPRAMOL - A PROGRAM FOR DETERMINATION OF INTERCALATED CRYSTAL STRUCTURES USING COMBINATION OF MOLECULAR SIMULATIONS AND POWDER DIFFRACTION.

Bohdan Koudelka, Pavla Čapková

Department of Chemical Physics and Optics, Faculty of Mathematics and Physics, Charles University Prague, Ke Karlovu 3, 121 16 Prague 2, Czech republic

Method of structure analysis of intercalates has been developed, using combination of molecular simulations with powder diffraction. Program Supramol for determination of intercalated structures uses the crystal energy minimisation in conjunction with powder diffraction data.

Program solves the multiple minima problem in molecular mechanics, generating systematically the initial models and searching for the global energy minimum by comparing the experimental and calculated diffraction pattern. Program is compatible with *Cerius2* modelling environment.

1. Introduction

Molecular simulations represent very powerful tool in analysis of structures with certain degree of disorder. In such a case it is usually not possible to produce single crystals of sufficient size and quality for conventional single crystal diffraction analysis. However the structure determination from powder diffraction data is complicated by large overlap of reflections and in addition by the structural disorder and preferred orientation of crystallites. Then the combination of molecular simulations with powder diffraction provides a route to crystal structure determination [1, 2, 3, 4].

In present work we used this method to solve the crystal structures of intercalates. Intercalates just belong to the structures, which are generally partially disordered and consequently the conventional diffraction analysis usually fails. In case of intercalates the host structure is built from rigid layers with covalent intralayer and weak interlayer bonding. Guest molecules intercalated into the interlayer space are non-covalently bonded to the host layers. The structure of intercalate is a result of competition between the host-guest and guest-guest non-covalent interactions.

Intercalation is in fact the positioning a known molecules into a known crystal structure, that means, the structure analysis of intercalates has to solve the specific problems:

- to find the position, orientation, arrangement and possible conformational changes of guest molecules in the interlayer space
- to describe the stacking of layers
- as the intercalated layered structure usually exhibit certain degree of disorder, the estimation of the character and degree of disorder is an integral part of their structure analysis

The energy minimisation routines employed by molecular mechanics simulations usually refine the starting geometry to a nearest local minimum, which is not necessarily the global minimum. The computational methods used to get the global minimum have to generate the large number of initial models with different starting geometry and can be divided into three groups [5]

- deterministic or rigid search by systematic scanning the entire potential energy surface
- stochastic methods (Monte Carlo)
- molecular dynamics.

Method presented in this paper is deterministic, using combination of molecular mechanics with experimental powder diffraction data. The strategy is based on the specific features of the intercalated structures, that means: the layers of the host structure and guest species are considered as a rigid units in the first approximation. If the IR spectroscopy does not confirm this assumption, then in the second stage the geometry of guest molecules can be refined. The series of initial models is created by systematic rotations and translations of guest molecules with respect to host layers and with respect to each other within one unit cell. Subrotations in guest molecules can also be included to allow torsions in bonding geometry. The X-ray powder pattern diffractogram is calculated for each initial model and compared with experimental data. The total sublimation energy consisting of van der Waals, electrostatic and hydrogen bond contribution is minimised only for the best fitting models. This method leads to a set of initial models which most accurately fit the experimental powder diffraction pattern. Finally, the disorder can be treated by an appropriate sum of the diffraction patterns correspondingly to the final minimised model, with nearly the same crystal energy.

2. How it works

At first we should index the peaks in diffraction pattern with appropriate h, k, l indices and determine the unit-cell parameters and space group of the crystal. This can be done by standard indexing procedures. We also have to determine the number of molecules in the unit cell. It can be assessed from density considerations or solid-state NMR [6]. Once the unit cell parameters, symmetry group and cell contents are known, we define a *grid of initial models* that covers the entire space given by all degrees of freedom i.e. positions, orientations and subrotations of intercalated molecules. Each node of this grid represents a single initial model of the structure we search.

X-ray patterns of all the initial models are compared with experimental one's. The chosen models, with the best agreement between experimental and calculated diffraction pattern, are then passed to energy minimisation within the one mesh of the grid.

The resulting structure with the lowest energy is then considered to be the global energy minimum. We can also compute the R_p factor to decide which model (from some group of models with quite low energy) fits best the diffraction data.

2.1 The grid of initial models

The rotations, subrotations and shifts of guest molecules in the unit cell are defined by relative position of selected atoms (e.g. rotation around C-C bond) or by static vector (e.g. rotation around x axes). Spherical coordinates (θ , φ) of rotations around point with relative definition of poles are also implemented.

If the best descriptions of desired movements and its ranges have been chosen for each intercalated molecule then we consider the size of the step of each movement with respect to the resulting number of initial models. Supramol can test about 10.000 models per second (Octane workstation with MIPS R10000 at 175MHz). Thus it is realistic to choose up to 10^8 - 10^{10} nodes of the grid. It allows two intercalated molecules in the unit cell to have a 5° - 10° step in angle variables and 0.1\AA step in shifts.

2.2 Fulfill the X-ray requirements

The intensities I_{hkl} of chosen reflection planes (heights of the peaks in diffraction pattern) in all the nodes of that grid can be calculated. Because the intensity

$$I_{hkl} = \sum_A \sum_B \sum_C \dots$$

is smooth function of all the movement variables (fractional coordinates u_A , v_A , w_A of each atom A in the unit cell), we are able to determine whether the experimental value of I_{hkl} can be reached within one mesh (multidimensional polyhedron) of the grid of the initial models. If it is so, the model is passed to energy minimisation.

2.3 Energy minimisation

At first approximation we minimise the structure energy with respect to Van der Waals (VdW) interactions (calculated using Lenard-Jones potentials) which defines a "good" packing of molecules within a unit cell. Only the models with VdW energy under e. g. 100 kcal/mol can be used as initial models for further Cerius² (or other more sophisticated) minimisation. For such a rough VdW calculations we use special fast algorithm.

This minimisation is applied to each node of the grid of models which satisfies the X-ray requirements. It is done only within the range of the size of one step of each molecular movement - the multidimensional polyhedron in the state space of crystal.

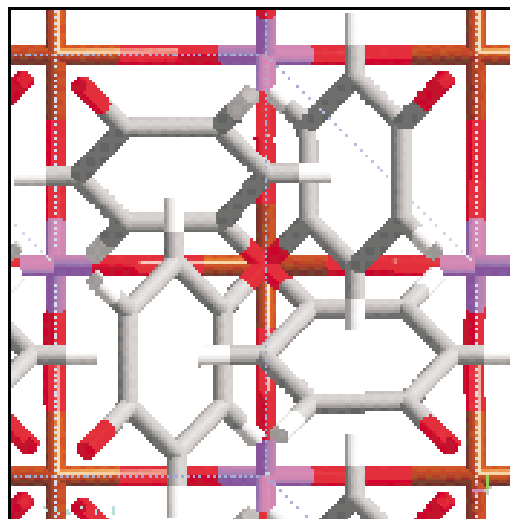


Figure 1. Phosphate intercalated with Benzochinon. The 4-fold axis of symmetry around Vanadium atom makes each of the Benzochinon position equivalent. In reality there is always one molecule, but in X-ray diffraction we must, because of the everaging, use all of the positions with occupancy factor 1/4. The crystal has $I4/m$ symmetry, the unit cell parameters $a = 6.21\text{\AA}$, $b = 6.21\text{\AA}$, $c = 20.18\text{\AA}$ and the density 2.30 g/m^3 .

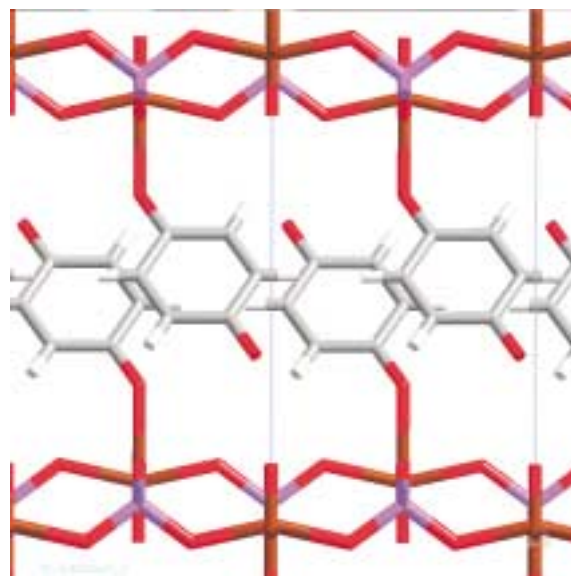


Figure 2. Phosphate intercalated with Benzochinon. Structure side view. The realistic model (only one of the four possible positions of Benzochinon presented) of mutual position of Benzochinon molecules with the smallest energy.

2.4 Using Supramol with Cerius²

The Supramol program was developed as an extension of the software package Cerius² but yet can work also as stand alone application. Both software packages communicates via *.msi and *.trj files. The relative definitions (with respect to selected atom positions) of movements of intercalated molecules can be done by MEASUREMENTS module in graphical Cerius² environment.

The set of the best initial models generated by Supramol is passed to the final crystal energy minimization using module Minimizer in Cerius². As a result we obtain the structure models corresponding to the lowest energy. Then

we use the R_p factor to decide which of the final models fits the experimental diffraction data.

2.5 VOPO₄ intercalated with Benzochinon

The program Supramol was successfully used to determine the crystal structure of Vanadyl Phosphate intercalated with Benzochinon.

To each Vanadium atom in the layer is anchored one molecule of Benzochinon. This way it fills the Vanadium incomplete octaeder. The symmetry of the layer and especially the 4-fold axis at Vanadium atom determines the symmetry of the whole intercalate. Each Benzochinon molecule than can be in four equivalent positions Fig. 2. This disorder makes the electron density function obtained from X-ray pattern rather fuzzy and unusable for determining the position of each individual atom in the unit cell.

The molecular modelling is often a good help in these cases. Thus we tried to set manually the initial model of the unit cell and minimise its energy by Cerius². It seemed impossible to fulfill the given X-ray pattern. Finally the program Supramol was successful at that task and we determined the structure which fits the experimental X-ray pattern by $R_p = 12\%$. The above pictures shows the obtained structure.

References

1. P. Erk, in: D. Braga et al. (eds.) *Crystal Engineering: From molecules and Crystals to Materials*, 143-161 (1999) Kluwer Academic Publishers.
2. H. R. Karfunkel, B. Rohde, F. J. J. Leusen, R. J. Gdanitz, G. Rihs, *Journal of Computational Chemistry* **14** (1993) 1125-1135.
3. G. E. Engel, S. Wilke, O. Konig, K. D. Harris, F. J. J. Leusen, *J. Appl. Cryst.* **32** (1999) 1169-1179.
4. R. B. Hammond, K. J. Roberts, R. Docherty, M. Edmondson, *J. Phys. Chem.* **B 101** (1997) 6532-6536.
5. Comba P.; Hambley T., W.(Ed.) VCH Verlagsgesellschaft mbH, Weinheim, New York, 1995 p.,1-58
6. J. M. Thomas, J. Klinovski, S. Rambadas, B. K. Hunter, *Chem Phys. Lett.* **102** (1983) 158-162.

EXPERIMENTAL DETERMINATION OF NET ATOMIC CHARGES AND CHARGE DENSITY DISTRIBUTIONS BY MEANS OF SINGLE CRYSTAL X-RAY DIFFRACTION

M. Šlouf

Department of Inorganic Chemistry, Faculty of Science, Charles University, Hlavova 2030, 128 40 Praha 2, Czech Republic

In crystals, X-rays are scattered mostly by electrons; scattering by the nuclei may be neglected. Due to strong attraction between the electrons and the nuclei, the maxima of electron density tend to coincide with nuclear positions.

Conventional X-ray structure determination relies on this fact and consists in localizing these maxima and assigning them to atoms. Typical result of the conventional structure determination is therefore complete information about nuclear positions or, in other words, the crystal structure.

Although most of the electron density in crystals is localized spherically around the nuclei, some electrons may be situated in bonding regions or nonbonding lone-pair orbitals. Nevertheless, the bonding effects are very fine: electron density maxima corresponding to the atoms of first row of the periodic table are about $1000 \text{ e}\text{\AA}^{-3}$, the changes in the electron density distribution due to bonding effects are three orders of magnitude lower, being about $1 \text{ e}\text{\AA}^{-3}$ [1]. Despite being small, the effects are observable. As the X-rays are scattered by all electrons, the information about the complete electron distribution must be included in the measured diffraction intensities.

Independent atom model. The assumption that the atomic electron density is well described by the spherically averaged density of the isolated atom has been the basis of X-ray structure analysis since its inception. This assumption implies that the crystal is composed of non-interacting neutral spherical atoms. The corresponding model is called Independent Atom Model (IAM). In fact all crystal structures were determined successfully by means of this model, which proves that it is indeed a good approximation. This can be justified by the fact that the great majority of the atomic electron density is spherically symmetric and a only a small part of the atomic electron density is non-spherical due to bonding effects as discussed in the previous paragraph. Within IAM it holds

$$\rho_{\text{atom}}(\mathbf{r}) = \text{spherically_symmetric_function}, \quad (1)$$

where $\rho_{\text{atom}}(\mathbf{r})$ is spherically averaged atomic electron density whose Fourier transform is atomic scattering factor of the isolated atom. Isolated atom atomic scattering factors are tabulated in the International Tables for Crystallography [2] and used in all routine X-ray structure determinations.

However, the lighter an atom, the worse the IAM approximation works. The lightest atom, hydrogen, has no inner shells of electrons, and thus the effect of bonding is relatively pronounced. Because of the overlap density in covalent X-H bonds ($X = \text{C}, \text{N}, \text{O}$), the mean of the hydrogen electron distribution is significantly displaced towards the X atom. If a spherical IAM hydrogen scattering factor is used in least-squares refinement, the hydrogen atom position is found at the maximum of electron density. As the maximum of electron density is shifted towards the relevant X atom, the result is *apparent shortening of the X-H bond*, which is far beyond the precision of X-ray structure determination [3]. Analogous effect connected with non-sphericity of the atom electron density distribution is called *asphericity shift*. The effect becomes visible if both X-ray and neutron diffraction data are available. Neutrons are diffracted by nuclei and so the neutron diffraction data are not biased by the electron density. X-rays are diffracted by electrons and within IAM it is assumed that the atom nuclei are located at the maxima of the electron density,

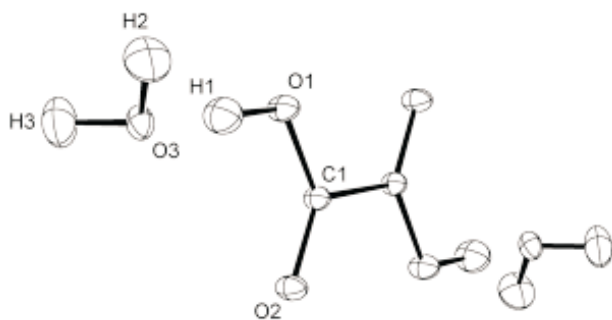


Figure 1. Crystal structure and atom labeling scheme of oxalic acid dihydrate. Thermal ellipsoids drawn at 50% probability level. Just atom of the asymmetric unit labeled. Source: ref. [10, 11].

which may not be always completely true. For example in water molecule the maximum of the oxygen atom electron density is shifted into the direction of the lone-pair density [4]. Asphericity shifts are observed especially for lighter atoms such as oxygen atom in oxalic acid -COOH group [5] or carbon atom in tetracyanoethylene -CN group [6]. Apparent shortenings of X-H may be as large as several tens of Å, whereas asphericity shifts much smaller, being typically just a few thousands of Å.

Another effects showing some limitations of IAM approximation are *existence of dipolar moments in crystals* and *occurrence of forbidden reflections* in diamond [7] or silicon [8].

κ-formalism. A simple modification of the IAM model, called κ-formalism [9], allows for charge transfer between atoms. By separating the scattering of the valence electrons from that of the core electrons, it becomes possible to adjust the population and radial dependence of valence shell. In practice, two charge-density variables, P_v and κ , are added to the conventional parameters of structure analysis. This model corresponds to the crystal consisting of spherical atoms, which can exchange electrons and change their size. Atomic electron density of an atom is described by

$$\rho_{\text{atom}}(r) = \rho_{\text{core}}(r) + P_v \kappa^3 \rho_{\text{valence}}(\kappa r), \quad (2)$$

where functions ρ_{core} and ρ_{valence} are spherically averaged core and valence electron density. Parameter r is distance from nucleus. Valence shell population parameter P_v gives the number of electrons in the valence shell; net atomic charge is calculated as $(N_v - P_v)$, where N_v is the number of valence electrons of the neutral atom. Radial expansion-contraction parameter κ allows expansion or contraction of the valence shell. If $\kappa > 1$, the same density is obtained at a smaller value of r , and the valence shell is therefore contracted. For $\kappa < 1$ it is expanded as the same density is found for bigger r . Functions ρ_{core} and ρ_{valence} have to be defined using chemical considerations before the least-squares refinement starts. Parameters P_v and κ are least-squares parameters, which are refined together with atomic positional and thermal displacement parameters. The least-squares refinement based on the κ-formalism is sometimes referred to as kappa refinement. Typical result of kappa refinement is in-

formation about net charges and expansion/contraction of the atoms (Table 1).

Multipole formalism. Within IAM and κ-formalism, the atomic electron density is still assumed to be spherical. However, some small part of the electron density in the crystal is not localized spherically around atomic nuclei, such as electron density of covalent bonds and lone electron pairs. Complete electron density distribution in the crystal must be described with more advanced models. The approaches that have become popular over the last 30 years are so-called *aspherical pseudoatom models*. After the first theoretical studies [12, 13, 14], the aspherical pseudo atom models were introduced into various programs. The majority of published electron density studies have been carried out with the following programs or program packages: LSEXP [14, 15], VALRAY [16], POP [17] and MOLLY [11]. Multipole model, which is a kind of aspherical pseudoatom model used by MOLLY, was had become probably the most popular and later it was introduced into modern program packages XD [18] and JANA2000 [19]. Multipole model is based on multipole formalism, which describes the atomic electron density as

$$\rho(r, \theta, \phi) = \rho_{\text{core}}(r) + \sum_{l, m} \kappa^l \rho_{\text{valence}}(\kappa r) P_l(\cos \theta) Y_l^m(\phi)$$

where ρ_{core} and ρ_{valence} are the spherically averaged core and valence electron density, respectively. The co-ordinates r , θ and ϕ refer to the local atom-centered Cartesian axes. R_l represents the Slater-type radial density functions. The angular density functions $d_{lm\pm}$ are real spherical harmonic functions and thus they are identical in shape to the atomic orbitals used in quantum chemistry. P_v is valence shell population parameter, from which net charge of an atom is obtained as $(N_v - P_v)$, where N_v is the number of electrons in the valence shell of the neutral atom in the ground state. $P_{lm\pm}$ are the multipolar population parameters. As long as the $P_{lm\pm}$ parameters equal zero, the atomic density is spherical; non-zero $P_{lm\pm}$ values change the atomic density to non-spherical. Parameters κ and κ' are the radial expansion-contraction coefficients of the perturbed density. Parameter κ is connected with expansion or contraction of the

Table 1. Typical kappa refinement result - net atomic charges of oxalic acid dihydrate. Crystal structure and atom labeling: Fig. 1. Source: ref. [10, 11].

atom	P_v	κ	net charge
C1	3.78(2)	1.056(3)	+0.22(2)
O1	6.31(1)	0.995(2)	-0.31(1)
O2	6.43(1)	0.988(2)	-0.43(1)
O3	6.41(2)	0.988(2)	-0.41(2)
H1	0.69(1)	1.2 (fixed)	+0.31(1)
H2	0.69(1)	1.2 (fixed)	+0.31(1)
H3	= H2	= H2	= H2

valence shell, parameter κ' is connected with expansion or contraction of multipolar functions. If κ is larger than one, the same density occurs at smaller r and thus the atom valence shell is contracted, and vice versa. Parameter κ' , describing expansion or contraction of multipolar functions, works in analogous way.

Functions ρ_{core} , $\rho_{valence}$, R_l and local atom-centered co-ordinate systems have to be defined for each atom before the least-squares refinement starts. Parameters P , κ , $P_{lm\pm}$ and κ' are treated as charge density variables in the least-squares refinement, which is often referred to as multipole refinement. The multipole refinement uses aspherical form factors corresponding to the atoms defined by Equation 3. The refined parameters, together with the density functions R_l and $d_{lm\pm}$ to which they refer, provide an analytical description of the electronic charge density. In other words, it is possible to plot model-based deformation electron density using the charge-density variables. The term deformation means that the map shows the deformations from spherical atomic density, such as covalent bonds and lone electron pairs (Figure 2). The model deformation electron density maps are typical result of the least-squares refinements based on aspherical pseudo-atom models.

In the world the charge density studies are more and more common [20]. In the Czech Republic the first charge density studies appeared probably in author's thesis [10]. Charge density studies at author's laboratory were performed at two levels: (1) net atomic charges were determined by means of kappa refinement and (2) complete charge density distribution in a crystal was determined by means of multipole refinement. In both oral presentation and poster, the results of several charge density studies performed at author's laboratory are given. Some other aspects of charge density studies, such as requirements on diffraction data quality, comparison of experimental and theoretical results and further possibilities of charge density studies are briefly discussed.

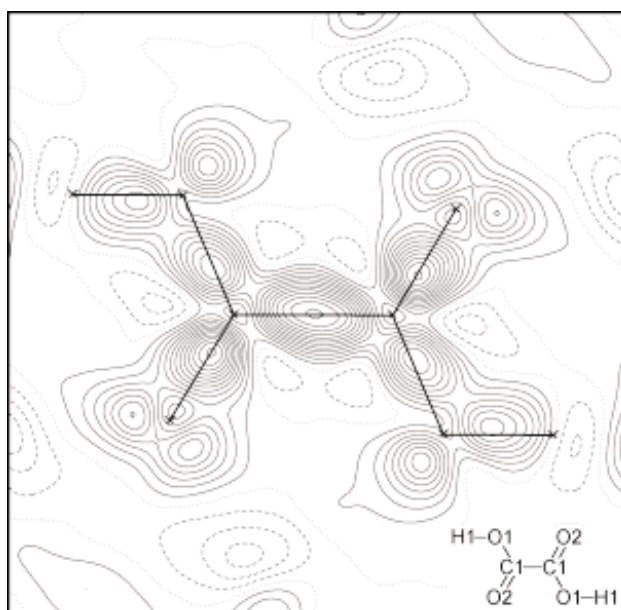


Figure 2. Typical multipole refinement result - dynamic model deformation electron density map of -oxalic acid dihydrate. Crystal structure and atom labeling: Figure 1. Source: ref. [10, 11].

References

1. Valvoda V.: *Experimentální metody studia pevných látek. Rentgenová difrakce: struktury, nábojové hustoty, vazby.* Vol. 3, edited by P. Lukáč, p. 41. Praha 1981. Matematicko-fyzikální fakulta UK.
2. *International Tables for Crystallography.* Vol. C, edited by A. J. C. Wilson. Dodrecht 1995. Kluwer.
3. Hanson, J. C., Sieker, L.C. & Jensen, L. H., *Acta Cryst.* **B29** (1973) 797-801.
4. Taylor, J. C. & Sabine T. M.: *Acta Cryst.* **B27** (1972) 134-139.
5. Coppens, P., Sabine, T. M., Delaplane, R. G. & Ibers, J. A.: *Acta Cryst.*, **B25** (1969) 2451-2457.
6. Becker, P., Coppens, P. & Ross, F. K.: *J. Am. Chem. Soc.*, **95** (1973) 7604-7610.
7. Nunes, A. C. (1971). *Acta Cryst.* **A27**, 219.
8. Trucano, P. & Batterman, B. W.: *Phys. Rev.* **B6** (1972) 3659-3662.
9. Coppens P., Guru Row, T. N., Leung, P., Stevens, E. D., Becker P. J. & Yang Y. W.: *Acta Cryst.* **A35** (1979) 63-72.
10. Šlouf, M: Disertace. Karlova univerzita, Praha 2001.
11. Hansen, N.K. & Coppens, P.: *Acta Cryst.* **A34** (1978) 909-921.
12. DeMarco, J. J. & Weis, R. J.: *Phys. Rev.* **A137** (1965) 1869-1871.
13. Dawson, B.: *Proc. Roy. Soc.* **A297** (1965) 264-288.
14. Hirshfeld, F. L.: *Acta Cryst.* **B27** (1965) 769-781.
15. Hirshfeld, F.L.: *Isr. J. Chem.* **16** (1965) 198-207.
16. Stewart, R. F.: *J. Chem. Phys.* **53** (1970) 205-213.
17. Epstein, J., Ruble, J.R. & Craven, B.M.: *Acta Cryst.* **B38** (1982) 140-146.
18. Koritsanszky, T., Howard, S., Su, Z., Mallinson, P. R., Richter, T. & Hansen, N. K.: *XD. Computer Program Package for Multipole Refinement and Analysis of Electron Densities from Diffraction Data.* Free University of Berlin, Germany 1997.
19. Petříček V. & Dušek M.: *JANA2000.* Institute of Physics, Praha, Czech Republic 2000.
20. Coppens, P.: *Acta Cryst.* **A54** (1998) 779-788

MAXIMUM ENTROPY METHOD IN STUDY OF ELECTRON DENSITIES

L. Palatinus and S. van Smaalen

Laboratory of Crystallography, University of Bayreuth, D-95440 Bayreuth, Germany

Introduction

The standard way of solving crystal structures from X-ray diffraction data is to approximate the electron density distribution (EDD) in the unit cell of the crystal by a model EDD, which is described by a relatively small number of parameters. Values of these parameters are then determined in order to give the best fit of the model EDD to the measured dataset. This is possible thanks to strong overdetermination of the problem, since for determining a few or few tens of parameters some hundreds or thousands reflections are available, and there is a finite number of best solutions, usually only one.

This is not the case if we want to describe the ED by its values in an arbitrarily dense grid in the unit cell. The number of values to be determined can now be much higher than the number of the data. In such case there is an infinite family of equally good solutions, and one needs some additional criterion, which allows choice of only one best solution. Treatment of this problem leads to the Maximum Entropy Method (MEM).

The principle of Maximum Entropy Method (MEM)

Although the MEM is very general principle applicable to nearly every field of scientific work [1], let us consider here explicitly the case of the X-ray scattering experiments. Suppose we have some information prior to using our experimental data. This information can be e.g. the number of electrons per unit cell and the dimensions of the unit cell, or we might already have some model of the structure, which we only want to refine. We can then construct some prior EDD, the most probable one subject to all prior information we have. In case of knowing only the number of electrons in the unit cell and cell parameters, the only information about the EDD we have is its average value, and the best EDD we can construct is the uniform or "flat" one, having in each point its average value. Constructing any other

EDD would mean including some other information we do not have any evidence form.

The basic principle of the searched selection criterion is then based on assumption that the best solution should not contain any information not contained in the data. In other words, the solution should describe the data, while being minimally deviated from the prior EDD, which we suppose to be most probable without using any experimental data. It is now desirable to find some measure of the "information contents" of the EDD. It can be shown [2,3] that the only function fulfilling all the necessary conditions is the one of the form

$$S = - \rho \int \frac{\rho}{\tau} \ln \frac{\rho}{\tau} dV$$

Here ρ_i denotes value of EDD in a grid point numbered by i , and τ_i denotes the value of the prior EDD at the same grid point. This function is called the (information) entropy for its formal (and in some sense factual, too) similarity to the thermodynamic entropy. This function has single maximum for $\rho = \tau$, where $S = 0$, and decreases monotonically in all directions. The lower value of entropy, the higher extra information contents of the corresponding ρ relatively to given τ .

As a result of previous paragraphs, the best solution is that one, which describes the data properly and has from all such solutions the maximum entropy. Since the data are supposed to be noisy with statistically Gaussian distribution of errors, the most probable solution is not the one corresponding exactly to the data, but the one, which satisfies the condition

$$\frac{F_{\text{obs}} - F_{\text{calc}}}{\sigma} = 0$$

Here F_{obs} denotes the observed structure factors, F_{calc} the structure factors calculated for the current estimate of the EDD, and σ is the standard error of F_{obs} . N_{obs} is the number of observed structure factors. F_{calc} can be calculated from any given EDD by its Fourier transform. Using this condition (called F-constraint) directly implies that the phases of all F_{obs} are known. It is possible to construct other constraints, which contain only amplitudes of structure factors or even only sums of amplitudes of several structure factors [4]. Nevertheless, these constraints cannot be used separately and some phase information is necessary in any case.

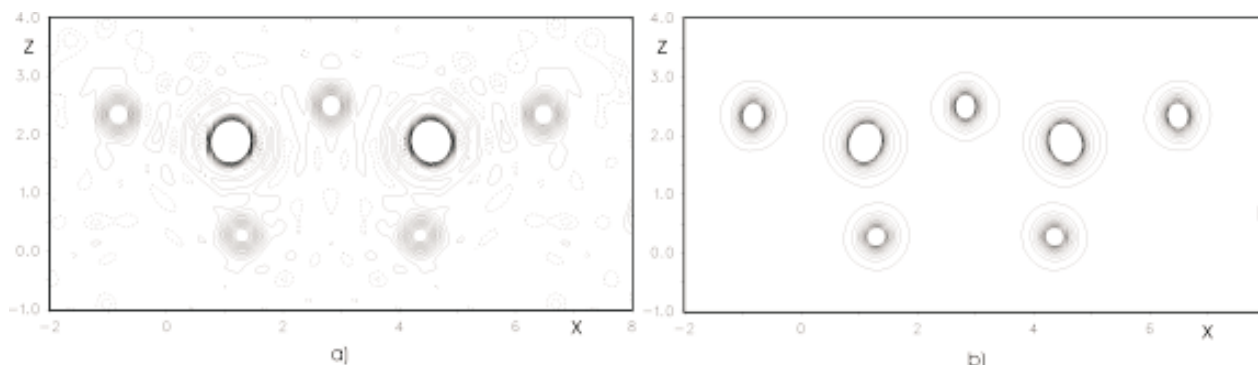


Figure 1. V_2O_5 group of α' - NaV_2O_5 compound, section parallel to 010 at $y = 0.25$. Lattice parameters $a = 11.311$, $b = 3.610$, $c = 4.802$. For both figures simulated data up to $\sin \theta/\lambda = 1.00$ were used. a) Result of Fourier transform. Positive contours full, interval $2e/\text{\AA}^3$. Negative contours dashed, interval $1 e/\text{\AA}^3$, zero contour omitted. Positive cut-off $30 e/\text{\AA}^3$. Maximum density $188.5 e/\text{\AA}^3$. b) Result of MEM. Contours like in Fig. 1a, no negative density. Maximum density $445.5 e/\text{\AA}^3$.

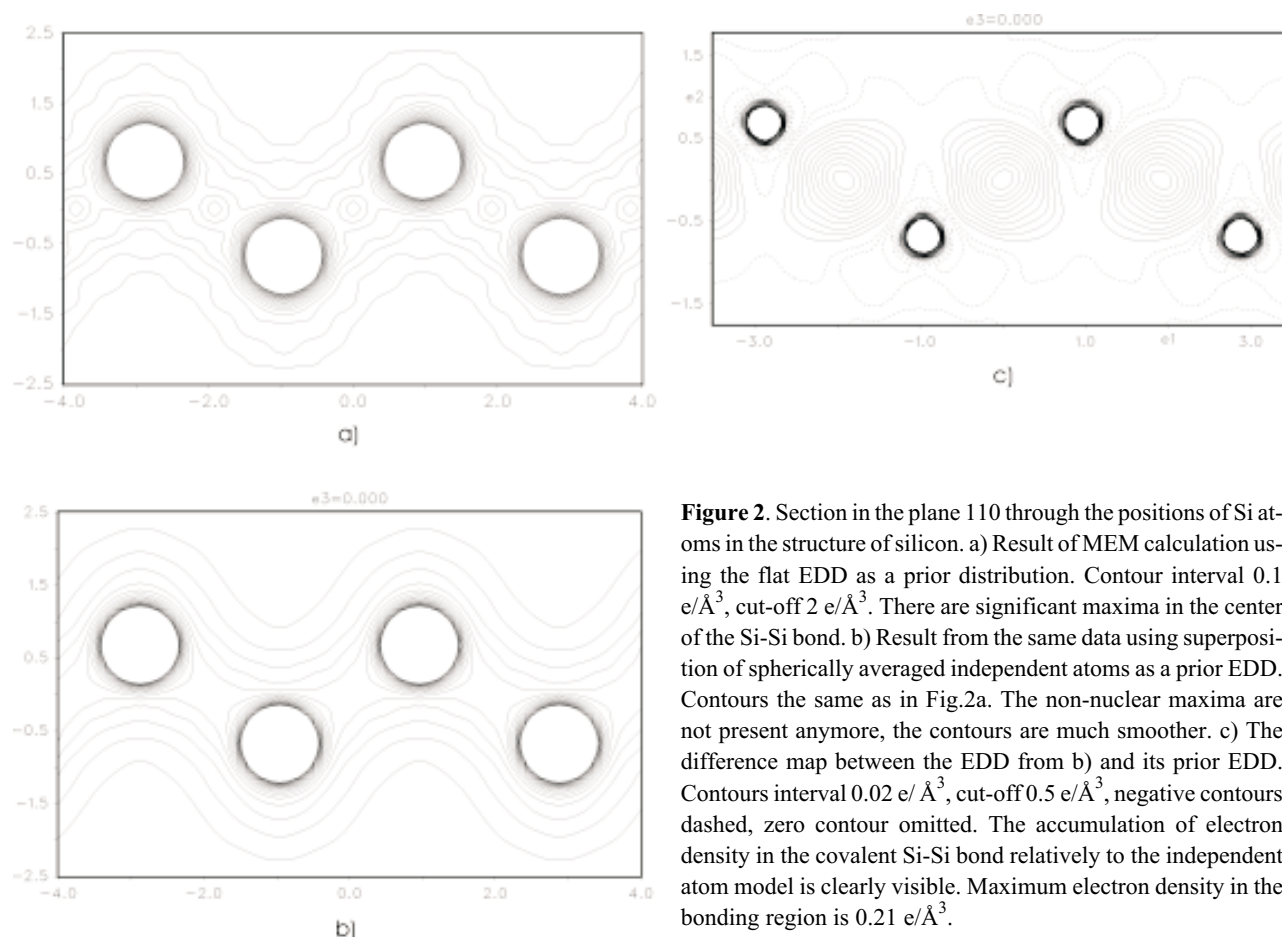


Figure 2. Section in the plane 110 through the positions of Si atoms in the structure of silicon. a) Result of MEM calculation using the flat EDD as a prior distribution. Contour interval $0.1 \text{ e}/\text{\AA}^3$, cut-off $2 \text{ e}/\text{\AA}^3$. There are significant maxima in the center of the Si-Si bond. b) Result from the same data using superposition of spherically averaged independent atoms as a prior EDD. Contours the same as in Fig.2a. The non-nuclear maxima are not present anymore, the contours are much smoother. c) The difference map between the EDD from b) and its prior EDD. Contours interval $0.02 \text{ e}/\text{\AA}^3$, cut-off $0.5 \text{ e}/\text{\AA}^3$, negative contours dashed, zero contour omitted. The accumulation of electron density in the covalent Si-Si bond relatively to the independent atom model is clearly visible. Maximum electron density in the bonding region is $0.21 \text{ e}/\text{\AA}^3$.

Having constructed any constraint C , we need to perform the constrained entropy maximization. Using the method of Lagrange undetermined multipliers, this is equivalent to unconstrained maximization of function

$$= -\lambda ,$$

where the Lagrange multiplier λ has just the value, which assures the constraint is satisfied. Differentiating the above equation with respect to i gives the condition

$$\frac{\partial}{\partial \rho} = \frac{\partial}{\partial \rho} - \lambda \frac{\partial}{\partial \rho} =$$

Using the definition of entropy, we get a solution in a form

$$\rho = \tau \quad -\lambda \frac{\partial}{\partial \rho} \div$$

This together with the constraint equation gives a set of $N+1$ nonlinear equations (N being the number of the grid points), which cannot be solved analytically. There are several algorithms, which solve the maximization problem iteratively [5].

MEM in practice

There are several problems, which cause MEM not being suitable for ab initio structure solution, except for rare simple cases. They are obvious from the definition of F-constraint [6]:

- The phases of F_{obs} must be known in advance.
- The assumption of Fourier transform relation between F_{obs} and corresponding ED neglects the effect of anomalous scattering. Especially for the heavier atoms this effect is not negligible, and the correction of the data is necessary. [7].
- The F_{calc} are computed as a Fourier transform of one unit cell, therefore the F_{obs} must be rescaled to this scale, too.

To solve any of these problems, one needs some input model. The model is usually taken from the standard refinement. The main advantage of using MEM is its ability to reveal more details in the resulting EDD and to go beyond the approximation of spherically averaged independent atoms used in standard refinement methods.

Example 1 – Alternative to the Fourier transform

The intrinsic property of EDD computed from structure factors by (inverse) Fourier transform is the presence of oscillations caused by assuming all non-measured structure factors being zero. The result can then contain physically unreasonable negative electron density and is full of artifacts. In opposite to that, the condition on the missing observations in the MEM is not in the reciprocal space, but in the direct space, and is given by forcing the result having maximum possible entropy (\sim maximal smoothness). As a result, MEM “finds” the values of missing structure factors so as to achieve this smoothness. The difference between the results of both methods is striking (Fig. 1).

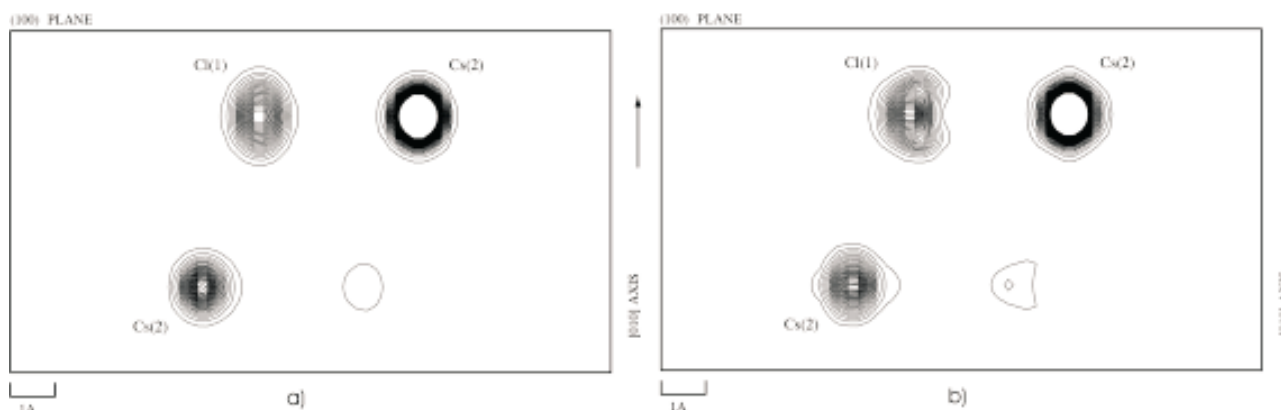


Figure 3. Section in the 100 plane of the Cs_2HgCl_4 structure at $x = 0.047$. Contour interval $1 \text{ e}/\text{\AA}^3$, cut-off $30 \text{ e}/\text{\AA}^3$. a) EDD corresponding to the standard refinement with only harmonic displacement parameters. b) MEM result from the same data. The anharmonic displacement of Cl(1) atom is clearly visible.

Example 2 – Silicon

The structure of silicon was studied by MEM using the dataset measured by very accurate Pendellösung method [8]. The result was quite shocking due to discovery of significant non-nuclear maxima in the EDD in the middle of the Si-Si bond [4](Fig. 2a). Later investigations [9] showed that these maxima are artifacts of the MEM and are not a real feature of silicon structure. This example shows the important role of the kind of the prior EDD used in MEM calculations (Fig. 2b). The difference map between the MEM result and the EDD created as superposition of spherically averaged atoms shows clearly the accumulation of electron density in the Si-Si bonding region (Fig. 2c).

Example 3 – Cs_2HgCl_4

The room temperature phase of this compound was studied by standard refinement methods and by MEM [7]. Contrary to the standard refinement using harmonic temperature factors, the MEM shows clearly the anharmonic displacement of the Cl atom (Fig. 3). This anharmonicity is

a precursor of the phase transition to lower symmetry at lower temperature.

References

1. B. Buck & V. Macaulay (eds.): *Maximum Entropy in Action*. Oxford 1991. Clarendon Press.
2. E.T. Jaynes: *Probability Theory: The Logic of Science*. , Fragmentary edition of March 1996
3. C.J. Gilmore, *Acta Cryst.*, **A52** (1996) 561-589
4. M. Sakata & M. Sato, *Acta Cryst.* **A46** (1990) 263-270
5. J. Skilling & R.K. Bryan, *Mon. Not. R. astr. Soc.*, **211** (1984) 111-124
6. M. Schneider & S. van Smaalen in W. von Linden et al. (eds.): *Maximum Entropy and Bayesian Methods*. Netherlands 1999. Kluwer Academic Publishers. 335-340
7. B. Bagautdinov, J. Luedecke, M. Schneider & S. van Smaalen, *Acta Cryst.* **B54** (1998) 626-634
8. T. Saka & N. Kato, *Acta Cryst.* **A42** (1986) 469-478
9. R.Y. de Vries, W.J. Briels, D. Feil, G. te Velde & E.J. Baerends, *Can. J. Chem.* **74** (1996) 1054-1058